MAGNETIC NATURE OF INTRINSIC CARBON DEFECTS

Petri Lehtinen

Laboratory of Physics
Helsinki University of Technology
Espoo, Finland

Dissertation for the degree of Doctor of Science in Technology to be presented with due permission of the Department of Engineering Physics and Mathematics, Helsinki University of Technology for public examination and debate in Auditorium E at Helsinki University of Technology (Espoo, Finland) on the 4th of March, 2005, at 12 o'clock noon.

Dissertations of Laboratory of Physics, Helsinki University of Technology
ISSN 1455-1802

Dissertation 129 (2005):
Petri Lehtinen: Magnetic Nature of Intrinsic Carbon Defects
ISBN 951-22-7520-1 (print)
ISBN 951-22-7521-X (electronic)

OTAMEDIA OY
ESPOO 2005

Abstract

Magnetism is a phenomenon that has been known for a very long time. Iron, cobalt, and nickel are known ferromagnetic materials. It is less known, probably because it is so unexpected, that even carbon can have ferromagnetic behaviour. Experimentally this has been confirmed on many occasions within the last decade. Ferromagnetic behaviour of carbon provides an example of the fact that magnetism is not well understood at the atomic scale. One of the aims of this thesis is to study and understand possible sources of ferromagnetism in carbon systems, thereby creating a possible foundation for the next generation of ferromagnets.

Carbon itself is a very interesting substance with numerous interesting properties. In the late 1980s and early 1990s new carbon allotropes were found, such as fullerenes (bucky balls) and nanotubes (cylinders), next to the old ones (graphite and diamond). Especially nanotubes have been considered as candidates for several future applications. Whatever the fabrication process, all allotropes of carbon will have intrinsic defects, and in this thesis the role of these defects in carbon magnetism is investigated in detail.

Studying magnetism requires "state-of-the-art"-methods due to the demand of high accuracy because energy differences between non-magnetic and magnetic cases are usually very small. *Ab initio* methods are usually the best for such studies, especially methods based on the density functional theory. Here, a state-of-art method which is based on the density functional theory and implementing projector augmented waves to model the properties of carbon is used.

Adatoms and vacancies are found to have magnetic moments of 0.5 μ_B and 1.0 μ_B, respectively. In practice, however, the high mobility of adatoms on graphene at room temperature would suggest that many of them recombine with vacancies or cluster together, destroying their magnetism. Despite the indications that a barrier to vacancy-interstitial pair recombination exists, efficient recombination seems to be confirmed by He-irradiation experiments. The magnetic signal was small despite the fact that the amount of defects created by the He ions is large. Also, the effect of the changing electronic structure on the magnetic moments of adatoms and vacancies is studied with the help of nanotubes. On nanotubes, the magnetism of an adatom decreases because of the curvature and differences in electronic structures while the magnetic moment of a vacancy in all but strongly metallic tubes is destroyed.

The experimental demonstration of induced ferromagnetism by proton irradiation on graphite indicates a promising direction for creating a magnetic carbon system in a controllable way. Simulations indicate that this is due to a combination of a hydrogen atom trapping at vacancies and pinning of mobile adatoms, producing magnetic C-H complexes and uncompensated vacancies.

Preface

This thesis has been prepared in the Laboratory of Physics in the Condensed Computational Matter and Complex Materials Group (Helsinki University of Techonology, Finland) during the years 2001-2004.

I wish to thank Academy Prof. Risto Nieminen for the opportunity of working in his group, advice, and ideas during this work. I also want to express my gratitude to my closest collaborators Dr. Adam Foster and Dr. Yuchen Ma for guidance. I would like to thank Prof. Kai Nordlund and Dr. Arkady Krasheninnikov for the collaboration. Thanks also to the colleagues and the personnel in the laboratory. I acknowledge the computing resources provided by Center for Scientific Computing.

Finally, I would like to thank my parents and brother for support.

Espoo, October 2004

Petri Lehtinen

Contents

List of Publications

This thesis consists of an overview and following publications:

I P. O. Lehtinen, A. S. Foster, A. Ayuela, A. V. Krasheninnikov, K. Nordlund, and R. M. Nieminen, *Magnetic Properties and diffusion of adatoms on a graphene sheet*, Physical Review Letters 91, 017202 (2003).

II A. V. Krashennikov, K. Nordlund, P. O. Lehtinen, A. S. Foster, A. Ayuela, and R. M. Nieminen, *Adsorption and migration of carbon adatoms on carbon nanotubes*, Physical Review B 69, 073402 (2004).

III P. O. Lehtinen, A. S. Foster, A. Ayuela, T. T. Vehviläinen, and R. M. Nieminen, *Structure and magnetic properties of adatoms on carbon nanotubes*, Physical Review B 69, 155422 (2004).

IV Y. Ma, P. O. Lehtinen, A. S. Foster, and R. M. Nieminen, *Magnetic properties of vacancies in graphene and single-walled carbon nanotubes*, New Journal of Physics 6, 68 (2004).

V P. O. Lehtinen, A. S. Foster, Y. Ma, A. V. Krasheninnikov, and R. M. Nieminen, *Irradiation-induced magnetism in graphite: a density-functional study*, Physical Review Letters 93, 187202 (2004).

The author has had an active role in all the phases of the research reported in this thesis. He has been involved in the planning of the calculations, analyzing the results and representing the interpretation. The author has written the main drafts for Publications I, III and V. The results calculated by the author provided a reference for the results presented in Publication II. In Publication IV the author took part in calculating results of the graphene part and in interpreting the overall results.

Chapter 1

Introduction

1.1 Carbon Atom and Hybridization

Carbon is a group IV element in the Periodic Table of the Elements with the chemical symbol C, its atomic number is six, and atomic weight 12.01 g/mol [1]. Carbon has four valence electrons in the $2s^2p^2$-configuration and two core electrons in the $1s$-orbital. In order to form bonds, the atoms' orbitals have to undergo a hybridization process, and carbon can have (acetylene) sp-, (graphite) sp^2-, and (diamond) sp^3-hybridizations while the other group four elements (Si,Ge, etc.) appear primarily in the sp^3-hybridization.

1.1.1 *sp*-Hybridization and Acetylene

In gas welding, acetylene (C_2H_2) is one of the two main gases, oxygen (O_2) is the other. In acetylene, carbons undergo a simple sp-hybridization (see Figure 1.1). A quantum mechanical description of the hybridization can be presented

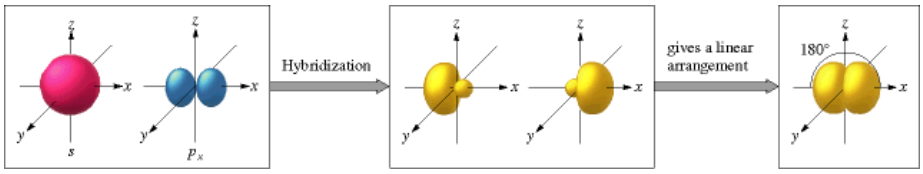

Figure 1.1: sp-hybridization [2].

as a linear combination of atomic orbitals. In the sp-hybridization, sp-orbitals can be presented as

$$\begin{aligned} |sp_a\rangle &= C_1|2s\rangle + C_2|2p_x\rangle \\ |sp_b\rangle &= C_3|2s\rangle + C_4|2p_x\rangle, \end{aligned} \tag{1.1}$$

where C_i:s are coefficients. These coefficents are determined from the requirements, which the orbitals must satisfy, namely $\langle sp_a|sp_b\rangle = \delta_{ab}$ (orthogonality and norm). Additionally, $|2s\rangle$ and $|2p_x\rangle$ can be presented in terms of $|sp_i\rangle$. The norm of $|2s\rangle$ and $|2p_x\rangle$ equals one. These conditions provide four equations for

the C_i:s, which are then

$$\begin{cases} C_1C_3 + C_2C_4 = & 0 \\ C_1^2 + C_2^2 = & 1 \\ C_2^2 + C_3^2 = & 1 \\ C_3^2 + C_4^2 = & 1. \end{cases} \tag{1.2}$$

Solving Equation (1.2) the result is

$$\begin{aligned} |sp_a\rangle &= \frac{1}{\sqrt{2}}\left(|2s\rangle + |2p_x\rangle\right) \\ |sp_b\rangle &= \frac{1}{\sqrt{2}}\left(|2s\rangle - |2p_x\rangle\right). \end{aligned} \tag{1.3}$$

The hybridized orbitals' property is that they are larger in amplitude in one direction and smaller in the other. The $|sp_a\rangle$ orbital is stronger or elongated in the positive x-direction while weaker or shrunk in the negative x-direction. If the nearest neighbor is then in the positive x direction, the overlap between suitably hybridized orbitals increases, resulting in lower total energies (this is also called as the σ bond). The remaining two electrons are perpendicular to the hybrid orbital, and they interact with p-orbitals of the nearest neighbor, and form a weaker bond known as the π-bond [3] (see Figure 1.2).

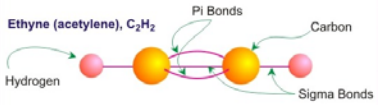

Figure 1.2: Schematic presentation of acetylene [4].

1.1.2 sp^2-Hybridization and Graphite

Pencils are probably the most commonly used application of graphite, which is composed of layered networks of hexagons. Layers are easily removed due to weak van der Waals bonds while the network is harder to break. Each carbon atom has three nearest neighbors in the plane, and the hybridization process, called sp^2-hybridization, is thus different from the one in acetylene (see Figure 1.3). In the sp^2-hybridization, three out of four carbon's valence electrons are involved in the mixing of orbitals, and the angle between the three orbitals is 120°. This means that the hybridized orbitals are in the directions (0,-1,0), ($\sqrt{3}$/2,1/2,0), and (-$\sqrt{3}$/2,1/2,0). The orbitals are then made as follows:

$$\begin{cases} |sp_a^2\rangle & = C_1|2s\rangle + \sqrt{1-C_1^2}|2p_y\rangle \\ |sp_b^2\rangle & = C_2|2s\rangle + \sqrt{1-C_2^2}\left[\frac{\sqrt{3}}{2}|2p_x\rangle + \frac{1}{2}|2p_y\rangle\right] \\ |sp_c^2\rangle & = C_3|2s\rangle + \sqrt{1-C_3^2}\left[-\frac{\sqrt{3}}{2}|2p_x\rangle + \frac{1}{2}|2p_y\rangle\right]. \end{cases} \tag{1.4}$$

From orthonormal requirements of $|sp_a^2\rangle$, $|2s\rangle$ and $|2p\rangle$, the constants (C_i) can be solved with results: $C_1 = C_2 = 1/\sqrt{3}$ and $C_3 = -1/\sqrt{3}$. A schematic presentation of different bonds in graphene (one layer of graphite) is presented in Figure 1.4

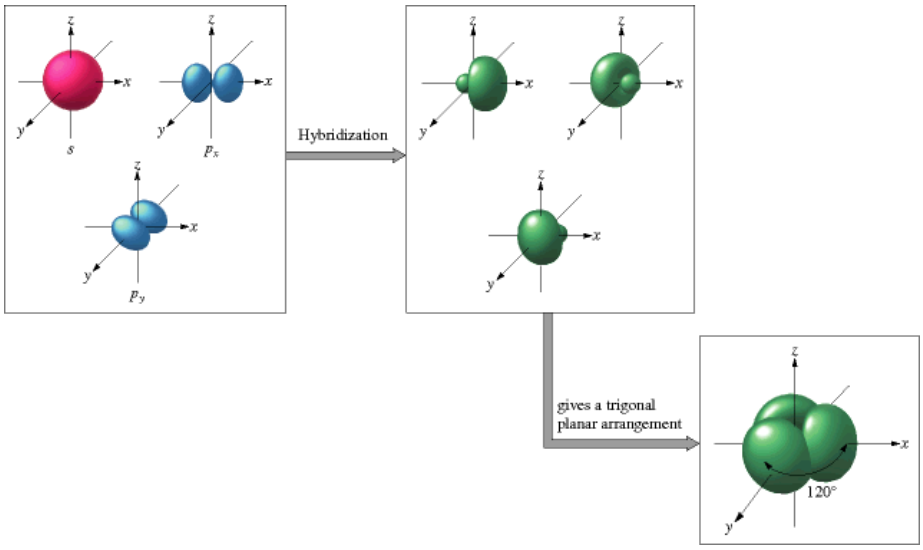

Figure 1.3: sp^2-hybridization [2].

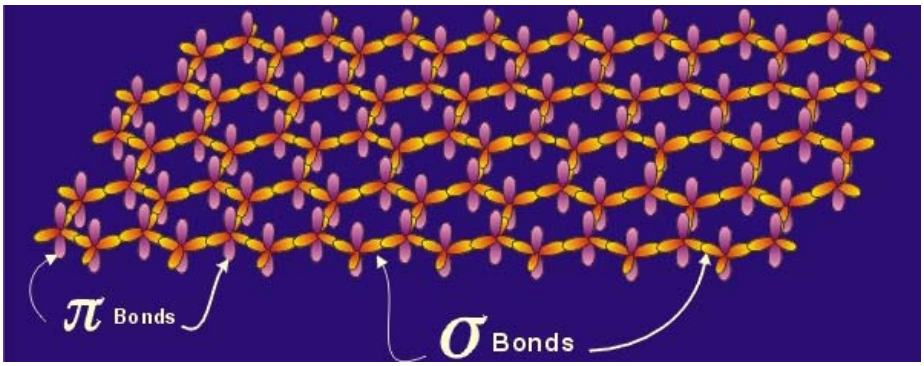

Figure 1.4: Schematic presentation of graphene [4].

1.1.3 sp^3-Hybridization and Diamond

In the sp^3-hybridization (see Figure 1.5) the directions of the bonds can be selected as (1,1,1), (-1,-1,1), (-1,1,-1), and (1,-1,1). The construction of the

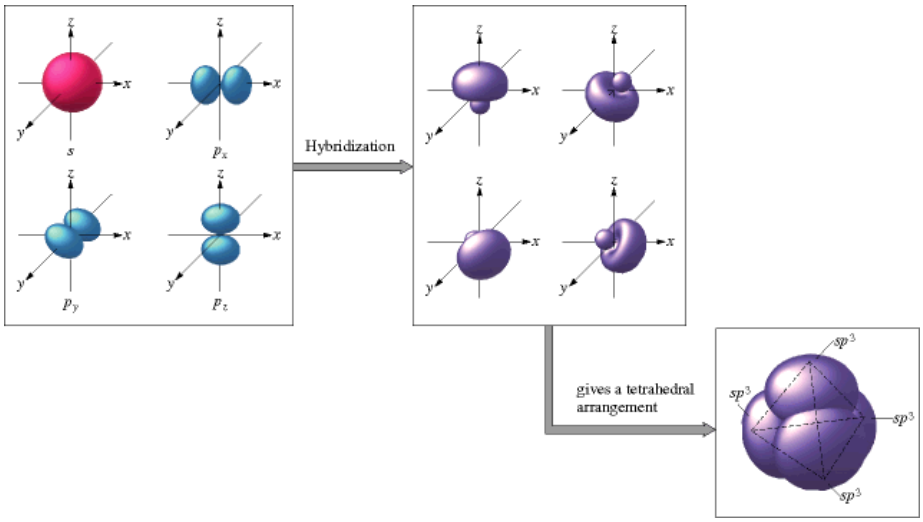

Figure 1.5: sp^3-hybridization [2].

orbitals is then comparable to the sp- and sp^2-hybridizations [3]. Diamond (Figure 1.6) is the best example of the material having this structure, and it is the hardest known material and the best heat conductor. It would also be the best semiconductor material if the doping of diamond was anything but impossible.

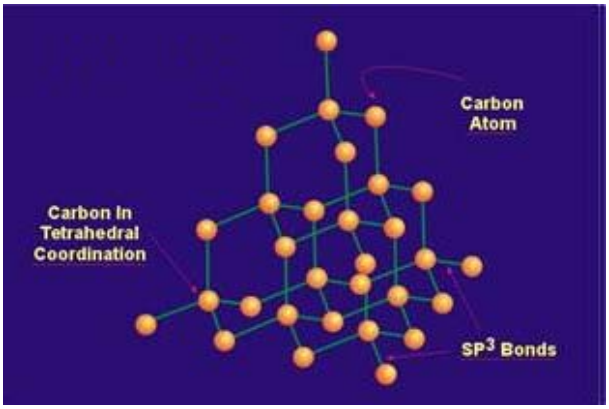

Figure 1.6: Schematic presentation of diamond [4].

In order to make a carbon-carbon bond, one $2s$-electron has to be excited to a $2p$-orbital. The energy required to make this transition is roughly 4 eV. The covalent bonding energy for σ-orbitals (3-4 eV per bond) is larger than $2s$-$2p$ energy separation. Also, it is important to note that the directions of the three wave functions in the sp^3-hybridization are freely determined while

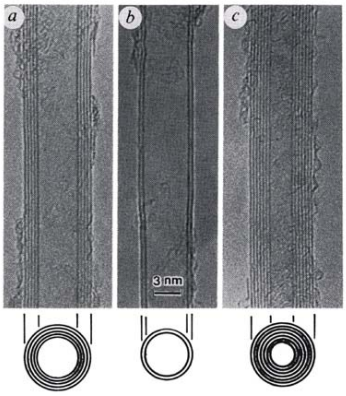

Figure 1.7: TEM images of multi-wall coaxial nanotubes with various inner and outer diameters, d_i and d_o, and numbers of cylindrical shells N: reported by Iijima using TEM: (a) N=5 d_o=67 Å,(b) N=2, d_o=55 Å, and N=7, d_i = 23 Å, d_o=65 Å. [5]

the fourth direction is determined by the orthonormality conditions imposed on the $2p$-orbitals. This fact gives rise to possible sp^2-hybridization of a planar pentagonal (or heptagonal) carbon ring, and $sp^{2+\eta}$-hybridization ($0 < \eta < 1$), which is found in fullerenes. It is expected that the $sp^{2+\eta}$ hybridization has a higher excitation energy than the symmetric sp^2-hybridization because of the electron-electron repulsion, which occurs in the hybridized orbital [3].

1.1.4 Nanotubes

Carbon nanotubes were discovered by Iijima in 1991 (see Figure 1.7 [5]). They are essentially single sheets of graphite (graphene) rolled into a cylinder. If there are nanotubes inside each other, these are called multi-wall nanotubes. The diameter of a single-wall nanotube is less than few hundred ångströms while the length scale is in the micrometer range.

The three most common methods to synthesize nanotubes are arc discharge, chemical vapour deposition (CVD), and laser ablation (vaporization). In the arc discharge method two graphite rods, which are a few millimeters apart, are connected to a power supply. Carbon atoms are vaporized into a plasma and nanotubes are formed at the rod connected to the negative electrode where 30 to 90% of the carbon consumed is converted to nanotubes. The single-walled nanotubes produced have diameters between 0.6-1.4 nm while multi-wall nanotubes' inner tube have diameter in range 1-3 nm and outer tube's diameter is approximately 10 nm. The tubes are short and they appear in random sizes and directions, which means that lot of purification is needed. With the arc discharge method single- and multi-wall nanotubes are easily produced, and they have few structural defects. In the CVD method, a substrate is placed in an oven, which is heated up to 600 °C and carbon bearing gas such as methane is slowly added. As the gas decomposes, carbon atoms are free and recombine into nanotubes. Typical yield is between 20-100%. Tubes are long with diameters of 0.6-4 nm in single-wall and 10-240 nm in multi-wall nanotubes. The CVD

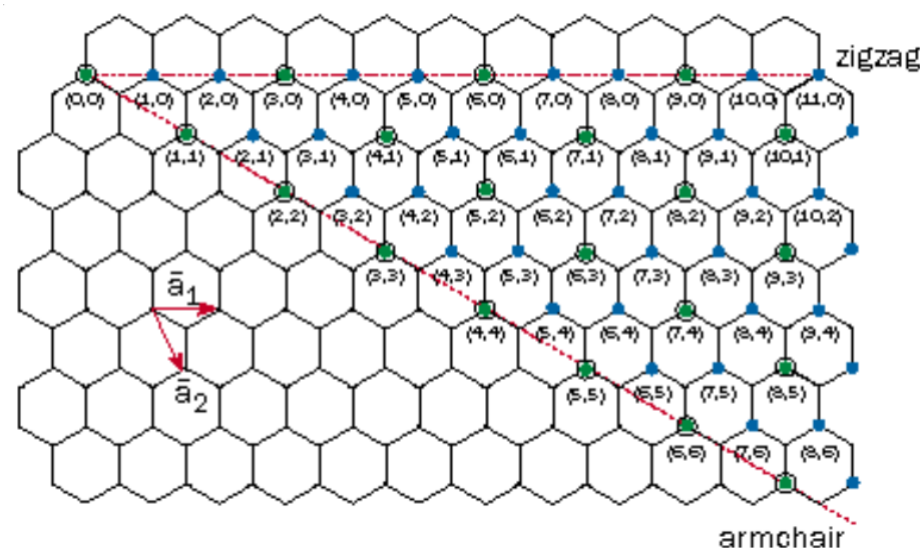

Figure 1.8: Chirality vector. The nanotubes having chirality vector marked with a green ball are metals in the sense of zone-folding. The rest are semiconductors. [7]

method is the best candidate for industrial purposes since the process is the easiest to scale up and simple. Single-wall nanotube's diameter can be controlled and resulting tubes are relatively pure. Most of the produced nanotubes are, however, multi-walled and riddled with defects. In the laser ablation method, graphite is heated with intense laser pulses. A pulsing lasergenerates carbon gas, from which the nanotubes are formed with up to 70 % yields. Single-wall tube bundles are long, 5-20 microns, and individual diameter varies between 1-2 nanometers. The diameter control is good and there are few defects. Synthesis of multi-wall nanotubes with this method is not too attractive since it is too expensive [3, 6].

The electronic structure of a nanotube depends on how it is rolled, and is designated by a pair of letters (n,m), which is also called the chirality vector. The meaning of these letters can be explained with the help of Figure 1.8. The chirality vector starts at (0,0) and ends at (n,m). Then combining the starting point and the end point we have a tube that we wanted. If the tube is designated as (n,0), the tube is called a zigzag nanotube. If the tube is of the form (n,n), the tube is an armchair nanotube. The rest in between are called achiral nanotubes. The determination of whether a tube is a metallic or semiconducting, is as follows: if $n - m$ is divisible by 3, the tube is metallic; otherwise it is semiconducting. This can be understood in terms of zone folding and analogy to graphite - the degenerate π and π^* bands (the asterisk stands for antibonding; usually not occupied, above the Fermi-level) in the graphite Brillouin zone are folded into the Γ point in a nanotube [8, 9, 10, 11]. However, this type of description does not take into account the effect of curvature. Due to the curvature of the nanotube, the π^* and σ^* orbitals hybridize, and thus a small gap opens in zigzag nanotubes. This effect is the strongest in nanotubes, which have radius less than that of C_{60} [3].

1.2 Intrinsic Magnetism in Carbon Systems

Observations of magnetism in various carbon systems [12, 13, 14] have stimulated much experimental and theoretical research work (Ref. [15] and references therein) on the magnetic properties of all-carbon systems. The driving force behind these studies was not only to create technologically important, light, non-metallic magnets with a Curie point well above room temperature, but also to understand a fundamental problem: the origin of magnetism in a system, which traditionally has been thought to show diamagnetic behavior only.

The question, which immediately springs to ones mind is whether magnetism is an intrinsic property of carbon systems or is due to the presence of magnetic impurities (e.g., Fe). The debate was initiated from the appearance of the two classic papers: in 2000 Kopelevich and coworkers published a paper [12] with an editor's note of the controversial nature of the result. In that work, the authors identified ferromagnetic and superconducting-like magnetization hysteresis loops in highly oriented pyrolytic graphite samples below and above room temperature. The conclusion was that magnetic impurities were extremely unlikely. In 2001 Makarova and coworkers [13] reported a discovery of strong magnetic signals in rhombohedral C_{60}. Their intention was to search for superconductivity in polymerized C_{60}; however, it appeared that their high-pressure, high-temperature polymerization process resulted in a magnetically ordered state. The material exhibited features typical of ferromagnets: saturation magnetization, large hysteresis and attachment to a magnet at room temperature. A careful analysis carried out in the original [13] and follow-up works [14, 16, 17] showed that one can exclude magnetic impurities as the origin of ferromagnetism.

If magnetism is indeed the intrinsic property of all-carbon systems, then the most important questions to be answered are as follows:

1. *What is the atomic structure of the magnetic phase and what is the local bonding geometry, which gives rise to the net magnetic moment?*

   The presence of local magnetic moments can explain only the paramagnetic behavior but not ferromagnetism. Thus, the second question is:

2. *How is the macroscopic ferromagnetic state formed and what is the mechanism of the long-range order formation?*

   Because ferromagnetic signals have been detected in various carbon systems such as graphite [12, 16], polymerized fullerenes [13], and carbon foam [14], it is highly important to understand:

3. *Is the mechanism of magnetic state formation common for all the carbon systems or is it different for different allotropes?*

   Finally, if magnetism is not the intrinsic property of all-carbon systems and it does not originate from magnetic impurities, then another question arises:

4. *Can magnetism result from impurity atoms, which are non-magnetic by themselves, but due to unusual chemical environment, e.g., due to bonding to defects in graphitic network, give rise to local magnetic moments?*

As for the first problem, a number of factors are nowadays thought to possibly give rise to the appearance of localized spins and the development of the magnetic state in all-carbon systems: defects in the atomic network such as under-coordinated atoms [18, 19, 20, 21, 22, 23], itinerant ferromagnetism [24, 25] and negatively-curved sp^2-bonded nano-regions in the carbon structures [14, 26]. Among these factors the defect-mediated mechanism appears to be the most general one because negatively-curved regions can hardly be found in graphite, and as for the second scenario, although itinerant mechanisms resulting from strong electron-elecron interactions and the effective dimensionality of the electron system can give rise to magnetism, direct experimental evidence supporting such a mechanism is still lacking.

The defect-mediated mechanism has been addressed in a considerable number of works [18, 19, 20, 21, 22, 23]. Although the details can be different for different carbon systems (polymeric fullerenes, graphite, nanotubes), the common feature is the presence of under-coordinated atoms, e.g., vacancies [21, 27], atoms on the edges of graphitic nano-fragments with dangling bonds either passivated with hydrogen atoms [22, 23, 28] or free [20, 23]. Structural defects, in general, give rise to localized electronic states, a local magnetic moment, flat bands associated with defects and thus to an increase in the density of states at the Fermi level, and eventually to the development of magnetic ordering. However, even if this conjecture is correct, it is not clear at all whether such defects are actually present, or if their concentration is high enough to provide the magnetic moment observed in the experiments.

At the same time, it is well known that irradiation of carbon systems with energetic electrons and ions should give rise to defects, and their number can be controlled by choosing the right irradiation dose, particle energy and irradiation temperature. Thus, if irradiation of the originally non-magnetic carbon samples gave rise to magnetism, this could be strong evidence for the defect scenario.

Graphite samples were recently irradiated with 1.5 MeV He and 2.25 MeV H ions [29]. It was found that proton bombardment produced a strong magnetic signal, while bombardment with helium ions produced a signal, which was only slightly larger than background.

To explain the irradiation-induced magnetism and shed light on the role of defects in all-carbon magnetism, the atomic structure and magnetic moment of various defects is studied in this thesis at the atomistic level within the framework of Density Functional Theory (DFT). The importance of the behavior of various point defects–vacancies, interstitials and more complicated aggregations, both intrinsic, and those, which can appear in carbon nanotubes and graphite under irradiation to properties of material is addressed. Not only magnetic, but also structural and other characteristics of the defects are described, such as formation energies and diffusivity. It is shown that under certain conditions the defects can indeed give rise to magnetism. Defects, which can appear under proton irradiation are considered, and the fact that even a small amount of hydrogen in carbon samples might be very important for the formation of the magnetic state is demonstrated.

Chapter 2

Introduction to Computational Methods

Modern atomistic modeling techniques can be divided into three parts [30]:

1. Molecular mechanics uses classical physics and is computationally cheap since it is very fast even with limited computer resources. It can be used to calculate large systems like enzymes, which may have thousands of molecules. This means that the primary users are in the area of biological physics. Molecular mechanics does not calculate electronic properties, which prohibits bond breaking. Instead, molecular mechanics requires *ab initio* or experimental data on which the force fields it uses are parameterized.

2. Semi-empirical methods use quantum physics but are computationally less demanding than *ab initio* methods. The idea is to use a relatively simple molecular-orbital theory to define the potential surface of interest in such a way that it can be adjusted to match *ab initio* calculations or experiment. The adjustments are usually made either by varying parameters that arise naturally in the semiempirical calculations or by adding locally defined correction functions to the semiempirical surface in order to "fix up" special regions of the potential surface such as barriers or minima [31]. This means the usage is in the medium sized systems with hundreds or even a few thousands of atoms. They too, however, rely on *ab initio* or experimental data.

3. *Ab initio* or "the first principles" methods are also based on quantum physics. They are mathematically very rigorous in the sense that they do not have empirical parameters. *Ab initio* methods are very useful for a broad range of systems. Computationally they are extremely expensive and this limits the size of the system to little over 100 atoms. The usage is in systems requiring high accuracy, and flexible atomic environments.

In the following studies *Ab initio* techniques are used by applying density functional theory (DFT) to find the ground state of the system. A brief outline of DFT is given by following closely Ref. [32].

2.1 Density Functional Theory

2.1.1 Basic Formalism

The Hamiltonian of an interacting many-particle system is

$$\hat{H} = \hat{T} + \hat{V} + \hat{W}, \tag{2.1}$$

which can be written in the second-quantized formalism as

$$\begin{aligned} \hat{H} = & \sum_{\alpha} \int d^3r \left[\hat{\psi}^{\dagger}_{\alpha}(\mathbf{r}) \left(-\frac{\hbar^2}{2m} \nabla^2 + v(\mathbf{r}) \right) \hat{\psi}_{\alpha}(\mathbf{r}) \right] \\ & + \frac{1}{2} \sum_{\alpha\beta} \int d^3r \int d^3r' \hat{\psi}^{\dagger}_{\alpha}(\mathbf{r}) \hat{\psi}^{\dagger}_{\beta}(\mathbf{r}') w(\mathbf{r}, \mathbf{r}') \hat{\psi}_{\beta}(\mathbf{r}') \hat{\psi}_{\alpha}(\mathbf{r}). \end{aligned} \tag{2.2}$$

In the nanometer scale, the dominant inter-particle interaction is the Coulomb interaction. The problem to solve, in general, is an eigenvalue problem, namely

$$\hat{H}|\Phi\rangle = (\hat{T} + \hat{V} + \hat{W})|\Phi\rangle = E|\Phi\rangle. \tag{2.3}$$

Assuming that the situation to deal with is such that the ground state is non-degenerate, a member $|\Psi\rangle$ belonging to family of $|\Phi\rangle$ provides the lowest eigenvalue ($|\Phi\rangle$ is a solution of the Schrödinger equation, $|\Psi\rangle$ is the one, which gives the lowest energy), i.e. the ground state energy:

$$\hat{H}|\Psi\rangle = E_{gs}|\Psi\rangle. \tag{2.4}$$

The ground state density can then be calculated from

$$\begin{aligned} n(\mathbf{r}) &= \langle\Psi| \sum_{\alpha} \hat{\psi}^{\dagger}_{\alpha}(\mathbf{r}) \hat{\psi}_{\alpha} |\Psi\rangle \\ &= N \sum_{\alpha} \int d^3x_2, ..., \int d^3x_N \, |\Psi(\mathbf{r}\alpha, x_2, ..., x_N)|^2, \end{aligned} \tag{2.5}$$

which is then a functional of $v(\mathbf{r})$; the idea was first presented in [33]. The particle number (N) and the ground state density ($n(\mathbf{r})$) are related through the configurational distribution function, which also gives one of the sum rules in the local density approximation (see appendix A).

The one to one correspondence between the density and the potential $v(\mathbf{r})$ is proved by first recognizing that two potentials, $\hat{V}$ and $\hat{V}'$, always lead to different ground states $|\Psi\rangle$ and $|\Psi'\rangle$ if the potentials differ more than a constant, i.e.

$$\hat{V} \neq \hat{V}' + \text{const.} \tag{2.6}$$

Eigenvalue equations for both potentials are

$$(\hat{T} + \hat{V} + \hat{W})|\Psi\rangle = E_{gs}|\Psi\rangle \tag{2.7}$$

and

$$(\hat{T} + \hat{V}' + \hat{W})|\Psi'\rangle = E'_{gs}|\Psi'\rangle. \tag{2.8}$$

If $|\Psi\rangle$ and $|\Psi'\rangle$ are the same, the result is

$$(\hat{V} - \hat{V}')|\Psi\rangle = (E_{gs} - E'_{gs})|\Psi\rangle, \tag{2.9}$$

which violates Equation (2.6). In the second phase of the proof, one must show that $|\Psi\rangle \neq |\Psi'\rangle$ implies $n(\mathbf{r}) \neq n'(\mathbf{r})$. Due to the Ritz principle

$$E_{gs} = \langle\Psi|\hat{H}|\Psi\rangle < \langle\Psi'|\hat{H}|\Psi'\rangle \tag{2.10}$$

and

$$\langle\Psi'|\hat{H}|\Psi'\rangle = \langle\Psi'|\hat{H}' + \hat{V} - \hat{V}'|\Psi'\rangle = E'_{gs} + \int d^3r\, n'(\mathbf{r})[v(\mathbf{r}) - v'(\mathbf{r})]. \tag{2.11}$$

The combination of (2.10) and (2.11) gives

$$E_{gs} < E'_{gs} + \int d^3r\, n'(\mathbf{r})[v(\mathbf{r}) - v'(\mathbf{r})]. \tag{2.12}$$

By writing the corresponding argument for E'_{gs}, using the assumption $n(\mathbf{r}) = n'(\mathbf{r})$, and adding with Equation (2.12) the result will be

$$E_{gs} + E'_{gs} < E_{gs} + E'_{gs}. \tag{2.13}$$

The statements of the Hohenberg–Kohn theorem can then be formulated as following:

- The ground state expectation value is a unique functional of the exact ground state density
$$\langle\Psi[n]|\hat{O}|\Psi[n]\rangle = O[n].$$

- Energy functional has variational character:
$$E_{v_0}[n] = \langle\Psi[n]|\hat{T} + \hat{W} + \hat{V}_0|\Psi[n]\rangle,$$
where $\hat{V}_0$ is the external potential of a specific system with ground state density $n_0(\mathbf{r})$ and ground state energy E_0. By virtue of the Rayleigh–Ritz principle $E_{v_0}[n]$ has the property
$$E_0 < E_{v_0}[n], \text{if } n \neq n_0 \tag{2.14}$$
and
$$E_0 = E_{v_0}[n_0]. \tag{2.15}$$
Hence, the ground state can be determined from
$$E_0 = \min_n E_{v_0}[n]. \tag{2.16}$$

- $\hat{T}$ and $\hat{W}$ do not depend on the $\hat{V}_0$ of the particular system, and hence, the total energy functional may be written as
$$E_{v_0}[n] = F_{HK}[n] + \int d^3r\, n(\mathbf{r})v_0(\mathbf{r}), \tag{2.17}$$
where
$$F_{HK} = \langle\Psi[n]|\hat{T} + \hat{W}|\Psi[n]\rangle.$$
Thus, F_{HK} is universal.

2.1.2 Kohn–Sham Scheme

The idea of creating something, which became to known as the Kohn–Sham equations [34] rose, according to Walter Kohn [35], from descriptional differences between the so-called Thomas-Fermi theory and the Hartree equations. The difference between those two theories was in the treatment of the kinetic energy term.

A system of N non-interacting particles described by the Hamiltonian

$$\hat{H} = \hat{T} + \hat{V}_S \tag{2.18}$$

has a unique total energy functional

$$E_S[n] = T_S[n] + \int d^3r\, v_S(\mathbf{r}) n(\mathbf{r}), \tag{2.19}$$

which has, according to the variational principle, the ground state density $n_S(\mathbf{r})$ corresponding to Equation (2.18). A central piece in establishing the Kohn–Sham scheme is that for any interacting system, there exists a local single-particle potential $v_S(\mathbf{r})$ such that the exact ground state density of the interacting system equals the ground state density of the non-interacting system, namely

$$n(\mathbf{r}) = n_S(\mathbf{r}).$$

The ground state density has then a unique representation (non-degeneracy assumed)

$$n(\mathbf{r}) = \sum_{i=1}^{N} |\psi(\mathbf{r})|^2 \tag{2.20}$$

in terms of the lowest single-particle orbitals obtained from the Schrödinger equation

$$\left(-\frac{\hbar^2}{2m}\nabla^2 + v_S(\mathbf{r})\right)\psi_i(\mathbf{r}) = \varepsilon_i\psi_i(\mathbf{r}), \varepsilon_1 \leq \varepsilon_2 \leq .... \tag{2.21}$$

Rewriting the total energy functional (2.17) into form

$$E_{v_0}[n] = T_S[n] + \int d^3r\, n(\mathbf{r})v_0(\mathbf{r}) + \frac{1}{2}\int d^3r \int d^3r'\, n(\mathbf{r})w(\mathbf{r},\mathbf{r}')n(\mathbf{r}') + E_{XC}[n] \tag{2.22}$$

the exchange-correlation functional $E_{XC}[n]$ is formally defined as

$$E_{XC}[n] = F_{HK}[n] - \frac{1}{2}\int d^3r \int d^3r'\, n(\mathbf{r})w(\mathbf{r},\mathbf{r}')n(\mathbf{r}') - T_S[n]. \tag{2.23}$$

The kinetic energy term in (2.22) has now changed from $T[n]$ to $T_S[n]$, which can be written in terms of single-particle orbitals

$$T_S[n] = \sum_{i=1}^{N} \int d^3r\, \psi^*(\mathbf{r}) \left(-\frac{\hbar^2}{2m}\nabla^2\right)\psi(\mathbf{r}). \tag{2.24}$$

Using the facts that Hohenberg–Kohn variational principle ((2.14),(2.15)) ensures that $E_{v_0}[n]$ is stationary for small variations δn around the minimum

density $n_0(\mathbf{r})$, single-particle orbitals satisfy Equation (2.21), and that the orbitals are normalized, an expression for single particle potential, which generates $n_0(\mathbf{r})$ via Equation (2.20) can be derived. The result is

$$v_{S,0}(\mathbf{r}) = v_0(\mathbf{r}) + \int d^3r'\, n_0(\mathbf{r}')w(\mathbf{r},\mathbf{r}') + v_{XC}([n_0];\mathbf{r}), \tag{2.25}$$

where

$$v_{XC}([n_0];\mathbf{r}) = \left.\frac{\delta E_{XC}[n]}{\delta n(\mathbf{r})}\right|_{n_0}. \tag{2.26}$$

2.1.3 Extension to Spin-Polarized Systems

In spin-polarized systems, $\hat{V}$ in (2.1) needs to be extended in general to

$$\hat{V} = \int d^3r\, [v(\mathbf{r})\hat{n}(\mathbf{r}) - \mathbf{B}(\mathbf{r})\cdot\hat{\mathbf{m}}(\mathbf{r})], \tag{2.27}$$

where the density operator is

$$\hat{n}(\mathbf{r}) = \sum_\alpha \hat{\psi}^\dagger_\alpha(\mathbf{r})\hat{\psi}_\alpha = \hat{n}_+(\mathbf{r}) + \hat{n}_-(\mathbf{r}) \tag{2.28}$$

and the magnetic moment density is

$$\hat{\mathbf{m}}(\mathbf{r}) = -\mu_0 \sum_{\alpha\beta} \hat{\psi}^\dagger_\alpha \sigma_{\alpha\beta}(\mathbf{r})\hat{\psi}_\beta, \tag{2.29}$$

where $\sigma_{\alpha\beta}$ is a Pauli spin matrix and in particular

$$\hat{\mathbf{m}}(\mathbf{r}) = -\mu_0(\hat{n}_+(\mathbf{r}) + \hat{n}_-(\mathbf{r})). \tag{2.30}$$

The difference of this formalism compared to the standard one is that instead of trying to find only the ground state density, the objective is to find a four vector $(n(\mathbf{r}), \mathbf{m}(\mathbf{r}))$ for the non-degenerate ground state. The one-to-one correspondence between the ground state and the ground-state densities can be established through a similar argument as in (2.10) and (2.11). This fact is enough to establish the variational principle. According to Ref. [32] there is not any proof that there is one-to-one correspondence between unique external potential $(v(\mathbf{r}), \mathbf{B}(\mathbf{r}))$ and a given ground state. However, in the limit $B \to 0$ this formalism leads to a suitable description of systems having a spin-polarized ground state even without an external magnetic field (and in this case one-to-one correspondence between external potential and the state holds, although, the z-component of magnetic moment can have either positive or negative sign).

2.1.4 Kohn–Sham Scheme in Spin-Polarized Systems

For later purpose, and for notational simplicity, the external magnetic field $\mathbf{B}(\mathbf{r})$, and magnetization $\mathbf{m}(\mathbf{r})$ have only z-components

$$\mathbf{B}(\mathbf{r}) = (0, 0, B(\mathbf{r}))$$

$$\mathbf{m}(\mathbf{r}) = (0, 0, m(\mathbf{r})).$$

The Kohn–Sham equation for the spin-polarized scheme consists of the following equations:

$$\left(-\frac{\hbar^2}{2m}\nabla^2 + v(\mathbf{r}) - \alpha\mu_0 B(\mathbf{r}) + \int d^3r'\, n_0(\mathbf{r}')w(\mathbf{r},\mathbf{r}') + v_{XC}([n_+,n_-];\mathbf{r})\right)\psi_i^{(\alpha)}(\mathbf{r}) = \varepsilon_i\psi_i^{(\alpha)}(\mathbf{r}),\ \varepsilon_i^{(\alpha)} \leq \varepsilon_2^{(\alpha)} \leq .... \tag{2.31}$$

where $\alpha = +\,\text{or}\,-$ and

$$n_\alpha(\mathbf{r}) = \sum_{i=1}^{\infty}\gamma_i^{(\alpha)}|\psi_i^{(\alpha)}(\mathbf{r})|^2, \tag{2.32}$$

with $\gamma_i^{(\alpha)}$ satisfying the following relations

$$\begin{aligned} \gamma_i^{(\alpha)} &= 1\,,\ \varepsilon_i^{(\alpha)} < \mu^{(\alpha)} \\ \gamma_i^{(\alpha)} &\leq 1\,,\ \varepsilon_i^{(\alpha)} = \mu^{(\alpha)} \\ \gamma_i^{(\alpha)} &= 0\ ,\varepsilon_i^{(\alpha)} > \mu^{(\alpha)} \\ \sum_{i=1}^{\infty}\gamma_i^{(\alpha)} &= N_\alpha\,,\ N_+ + N_- = N. \end{aligned} \tag{2.33}$$

The exchange-correlation potentials are defined as

$${v^{(\alpha)}}_{XC}([n_+,n_-];\mathbf{r}) = \left.\frac{\delta E_{XC}[n]}{\delta n_\alpha(\mathbf{r})}\right|_{n_0}, \tag{2.34}$$

and the functional $E_{XC}[n_+,n_-]$ is defined as

$$E_{XC}[n] = F_L[n_+,n_-] - \frac{1}{2}\int d^3r \int d^3r'\, n(\mathbf{r})w(\mathbf{r},\mathbf{r}')n(\mathbf{r}') - T_L[n_+,n_-]. \tag{2.35}$$

$F_L[n_+,n_-]$ is an extension of F_{HK} to include degenerate states and constrained search, whereas T_L can be written as

$$T_L[n] = \sum_{i=1}^{N}\gamma_i^{(\alpha)}\int d^3r\,\psi_\alpha^*(\mathbf{r})\left(-\frac{\hbar^2}{2m}\nabla^2\right)\psi_\alpha(\mathbf{r}). \tag{2.36}$$

2.2 Approximations in DFT

2.2.1 Approximation for Exchange-Correlation Functional

Local (Spin) Density Approximation

One problem of the density functional theory is that the exchange-correlation energy functional defined in (2.35) is not known. E_{XC} is composed of the kinetic energy part and the interaction part. With the help of Equation (2.2) a few words can be said of the interaction part, which is the one that usually is divided into the exchange and correlation parts. With the help of Wick's theorem, an expansion of the expectation value into direct and exchange parts can be made.

In the homogeneous electron gas model (rotational and translational symmetry, ion cores considered as neutralizing background) the direct part cancels along with the contributions from the background and electron-background interaction to the total energy. So the problem is to study the exchange term perturbatively. The exchange term (in terms of Feynman diagrams, see Figure 2.1(a)) in the first order produces the well-known result for the exchange energy

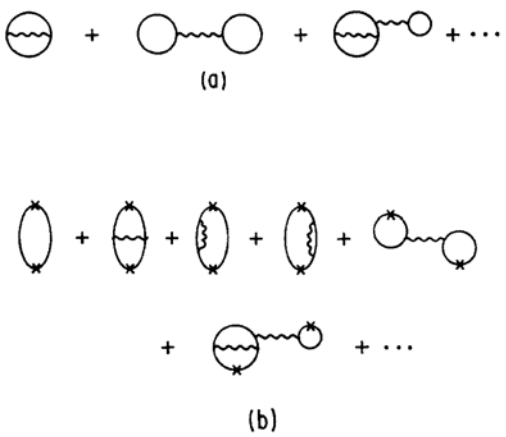

Figure 2.1: (a) Hartree-Fock energy diagrams. Because of the translational symmetry and the uniform charge background, only the first diagram is nonzero for a uniform electron gas. (b) The first diagram gives the second order perturbation on the kinetic energy. Each cross represents a density vertex with the momentum of the external field. [36]

$$\frac{E_x}{N} = -e^2 \frac{3}{4\pi} \left(3\pi^2 n\right)^{1/3} \frac{1}{2} \left[(1+\xi)^{4/3} + (1-\xi)^{4/3}\right], \tag{2.37}$$

where $\xi = (N_+ - N_-)/N$ [37]. The second order diagrams contributing to the exchange-correlation energy can be found in Figure 2.2. Figure 2.2(a) is well behaved (see for example Ref. [37]) while 2.2(b) is divergent. In higher order terms, contribution from diagrams resembling Figure 2.2(b) are the fastest diverging. In the high density limit, a summation of the fastest diverging terms can be done exactly [38, 39]. In the low-density limit, energy per particle can be computed exactly [40, 41, 42], from which the correlation contribution can be calculated. The remaining task is to find an expression for arbitrary density and spin-polarization. One of the most noteworthy parameterizations can be found in Ref. [43] where the high-density limit of electron gas, scaling relation of spin-polarized ring approximation and Monte-Carlo results by Ceperley and Alder [44] are taken into account [32]. The method described above is known as the local density approximation (LDA) or the local spin-polarized density approximation (LSDA). LDA has been highly successful because it fulfills the so-called sum rules of the exchange-correlation hole. Its deficiencies are that it inadequately cancels the self-interaction contributions. The consequence is that the local exchange-correlation potential does not exhibit correct asymptotic behavior proportional to $1/r$ for localized systems (atoms, molecules etc.).

(a) (b)

Figure 2.2: Second order diagrams contributing to exchange-correlation energy. Fig. (a) is the second order exchange contribution and well behaving while Fig. (b) is the first order correlation diagram contributing to the correlation energy.

Generalized Gradient Approximation

In order to improve LDA/LSDA the simplest thing to do is to include gradient terms of the density into the functional. The functional built is known as the gradient expansion approximation (GEA). The difference between LDA and GEA is that instead of being free particles and holes in Figures 2.1 and 2.2, they are experiencing an external potential. This modifies the calculation of the correlation energy in the high density limit [36]. In later work, it was realized that GEA violates the sum rules of the exchange-correlation hole. In order to enforce the sum rules of the exchange hole, a real space cut-off was introduced [45]. A similar treatment had to be done also for the correlation energy functional [46] since the exchange and correlation have to be treated in a balanced way. This leads to a scheme known as PW91 [47]. A useful formula in visualizing and thinking about the nonlocality, or in comparing one GGA with another is

$$E_{xc}^{GGA}[n_\uparrow, n_\downarrow] \approx \int d^3r\, n \left(-\frac{c}{r_s}\right) F_{xc}(r_s, \xi, s), \tag{2.38}$$

where $c = (3/4\pi)(9\pi/4)^{1/3}$, and $-c/r_s = e_x(r_s, \xi = 0)$ is the exchange energy per electron of a spin-unpolarized uniform electron gas, and F_{xc} is an enhancement factor showing the effects of the correlation [48].

The problem with LDA/LSDA and GGA is that they are both designed for non-homogeneous electron gases. Hence, the long-range interaction of non-overlapping systems is neglected. The reason for this is that the integrals involved in the evaluating the diagrams shown in sub-subsection 2.2.1 are done either in **k**-space (for Fourier transforms a box is needed) or in the real space with a regularization (potential of the form $exp[-\lambda r]/r$). This means van der Waals interactions (long range dipole-dipole interaction) are neglected and the calculation of distance between the layers of graphite can not be correctly done. Recently, a work has begun to overcome this problem (see for example Refs. [49] and [50]).

2.2.2 Band Gap Problem

The definition of the exact band gap Δ is [32]

$$\Delta = I - A \tag{2.39}$$

where I is the ionization potential

$$I = E(N-1) - E(N), \tag{2.40}$$

where $E(N)$ refers to the energy (functional) of N particle system, and A is the electron affinity

$$A = E(N) - E(N+1). \tag{2.41}$$

The definition of the chemical potential μ is

$$\frac{\delta E_v[n]}{\delta n(\mathbf{r})} = \mu. \tag{2.42}$$

If n_N is the ground state density of N particle system then the ground state energy can be written as $E_N = E_v[n_N]$. The exact chemical potential can then be written as

$$\mu(N) = \frac{\partial E_N}{\partial N}, \tag{2.43}$$

and with the help of the fractional particle formalism [32]

$$\mu(N) = \begin{cases} -I(Z) & \text{when } Z-1 < N < Z; \\ -A(Z) & \text{when } Z < N < Z+1. \end{cases} \tag{2.44}$$

This means that the band gap can be written in the form

$$\begin{aligned} \Delta = -\mu(N-\delta) - \mu(N+\delta) &\overset{(2.42)}{=} \left\{ \frac{\delta E_v[n]}{\delta n(\mathbf{r})}\bigg|_{N+\delta} - \frac{\delta E_v[n]}{\delta n(\mathbf{r})}\bigg|_{N-\delta} \right\}_{n=n_0} \\ &\overset{(2.22)}{=} \left\{ \frac{\delta T_S[n]}{\delta n(\mathbf{r})}\bigg|_{N+\delta} - \frac{\delta T_S[n]}{\delta n(\mathbf{r})}\bigg|_{N-\delta} \right\}_{n=n_0} + \left\{ \frac{\delta E_{xc}[n]}{\delta n(\mathbf{r})}\bigg|_{N+\delta} - \frac{\delta E_{xc}[n]}{\delta n(\mathbf{r})}\bigg|_{N-\delta} \right\}_{n=n_0} \\ &\equiv \Delta_{KS} + \Delta_{xc}. \end{aligned} \tag{2.45}$$

In order to recognize the terms in Equation (2.45) the fractional particle formalism has to be used with the fact that the chemical potential can be written as in Equation (2.42). First the Kohn–Sham total energy functional for $N+\delta$ particles can be written as

$$\begin{aligned} \Omega_0^+(\delta) = \sum_{i=1}^{N} \varepsilon_i + \delta\varepsilon_{N+1} - \frac{1}{2}\int d^3r \int d^3r'\, n^\delta(\mathbf{r}) w(\mathbf{r},\mathbf{r}') n^\delta(\mathbf{r}') \\ + E_{XC}([n^\delta]) - \int d^3r\, v_{XC}([n_0^\delta];\mathbf{r}) n^\delta(\mathbf{r}), \end{aligned} \tag{2.46}$$

and a similar equation for the $N-\delta$ particles

$$\begin{aligned} \Omega_0^-(\delta) = \sum_{i=1}^{N-1} \varepsilon_i + (1-\delta)\varepsilon_N - \frac{1}{2}\int d^3r \int d^3r'\, n^{-\delta}(\mathbf{r}) w(\mathbf{r},\mathbf{r}') n^{-\delta}(\mathbf{r}') \\ + E_{XC}([n^{-\delta}]) - \int d^3r\, v_{XC}([n_0^\delta];\mathbf{r}) n^{-\delta}(\mathbf{r}). \end{aligned} \tag{2.47}$$

Subtracting Ω_0 from Equation (2.46), and from Ω_0 Equation (2.47), the result is

$$\Omega_0^+(\delta) - \Omega_0 = \delta\varepsilon_{N+1} + (E_{XC}([n^{\delta^+}] - E_{XC}[n]) \tag{2.48}$$

and

$$\Omega_0 - \Omega_0^-(\delta) = \delta\varepsilon_N + (E_{XC}[n] - E_{XC}[n^{-\delta}]) \tag{2.49}$$

since the other terms explicitly depend on the density and a small density change around the ground state density does not change them. Dividing then Equations (2.48) and (2.49) with δ, taking δ to zero and subtracting them from each other an equation corresponding to Equation (2.45) is obtained. The final result will be then

$$\Delta = \varepsilon_{N+1} - \varepsilon_N + \left.\frac{\partial E_{XC}[n^\delta]}{\partial n}\right|_{N+\delta} - \left.\frac{\partial E_{XC}[n^\delta]}{\partial n}\right|_{N-\delta}. \tag{2.50}$$

If Δ_{xc} (ie. a discontinuity of derivative of $\mu(N)$ at $N = Z$) is the reason for the band gap problem, then changing the exchange-correlation functional does not improve the situation. The visible improvement is only a fluke since the underlying reason behind the gap is still present.

A partial remedy to the question, which of the deltas is responsible for the gap was given by Godby, Schüter and Sham [51]. They calculated the exchange-correlation from equation [32]

$$\begin{aligned} &\int d^3y\, v_{XC}(\mathbf{y}) \int \frac{d\omega}{2\pi}\, G_s(\mathbf{r},\mathbf{y};\omega) G(\mathbf{y},\mathbf{r};\omega) \\ &= \int d^3y \int d^3y' \int \frac{d\omega}{2\pi} G_s(\mathbf{r},\mathbf{y};\omega)\Sigma_{xc}(\mathbf{y},\mathbf{y}';\omega)G(\mathbf{y}',\mathbf{r};\omega), \end{aligned} \tag{2.51}$$

where $\Sigma_{xc}(\mathbf{y},\mathbf{y}',\omega)$ is the irreducible self-energy, from which the local Hartree potential has been substracted. G_s satisfies equation

$$(\omega - h_s)G_s = 1, \tag{2.52}$$

where h_s is the Kohn–Sham Hamiltonian. The full Green's function can then be written by means of Dyson's equation

$$G = G_s + G_s\tilde{\Sigma}G, \tag{2.53}$$

where $\tilde{\Sigma}$ is defined as

$$\tilde{\Sigma} = \Sigma_{xc}(\mathbf{y},\mathbf{y}';\omega) - \delta(\mathbf{r}-\mathbf{r}')v_{XC}(\mathbf{r}). \tag{2.54}$$

The connection to the particle density is

$$n(\mathbf{r}) = -i\int \frac{d\omega}{2\pi}\, G_s(\mathbf{r},\mathbf{r};\omega) = i\int \frac{d\omega}{2\pi}\, G(\mathbf{r},\mathbf{r};\omega). \tag{2.55}$$

Using the GW approximation for the self energy in (2.51), Godby, Schüter, and Sham found an agreement between v_{XC} in the local density approximation and v_{XC} obtained in the fashion of Equations (2.51)-(2.55), as well as for the band-structures. The consequence is that the neglected discontinuity is the primary source of error. For example, in the case of GaN the calculated band gaps (as in Ref. [52]) are between 1.76 eV and 3.0 eV in LDA calculations, and 1.45 eV in the GGA calculation compared to the experimental 3.41-3.65 eV.

2.2.3 Plane Wave Basis Set and Supercell Approximation

In electronic structure calculations, beside the exchange correlation energy, some things have to be approximated or assumed. In the following, a brief outline of these technical issues is given.

In the preceding sections, it was shown how a many-particle problem can be reduced to the effective single particle calculations. When looking at solids, the scale of the system is 10^{23} atoms. Even with non-interacting electrons, calculating their movement in that external potential would be a huge task. There are two challenges: a wave function must be calculated for each of the almost infinite number of electrons in the system and since each electronic wave function extends over the entire solid the basis set required to expand each wave function is almost infinite. With the help of the Bloch's theorem the wave function can be divided into a cell-periodic part and wavelike part [53], namely

$$\psi_i(\mathbf{r}) = \exp[i\mathbf{k}\cdot\mathbf{r}]f_i(\mathbf{r}), \tag{2.56}$$

where the cell-periodic part of the wave function can be expanded using a basis set consisting of a discrete set of plane waves whose wave vectors are reciprocal lattice vectors of the crystal

$$f_i(\mathbf{r}) = \sum_G c_{i,G}\exp[i\mathbf{G}\cdot\mathbf{r}]. \tag{2.57}$$

The wave function can therefore written as

$$\psi_i(\mathbf{r}) = \sum_G c_{i,G}\exp[i(\mathbf{k}+\mathbf{G})\cdot\mathbf{r}]. \tag{2.58}$$

Electronic states are allowed only at a set of $\mathbf{k}$ points determined by the boundary conditions in the bulk. The infinite number of electrons in the solid are accounted by an infinite number of $\mathbf{k}$ points, and only a finite number of electronic states are occupied at each $\mathbf{k}$ point. Each electron in an occupied state contribute to the total energy and thus the number of needed $\mathbf{k}$ points is infinite. Luckily, if the $\mathbf{k}$ points are close to each other the wave functions will be almost identical. This means that the wave function at one $\mathbf{k}$ point presents the wave functions in the region of space. In order to calculate the electronic potential and determine the total energy of the solid only finite amount of $\mathbf{k}$ points is required. Methods for approximating the electronic potential and total energy from filled electronic bands by calculating the electronic states at special sets of $\mathbf{k}$ points in the Brillouin zone have been presented for example in Refs. [54]. In metals, a large amount of $\mathbf{k}$ points is needed while in insulators only few to get good $\mathbf{k}$ point convergences.

When operating in $\mathbf{k}$ space, the terms with small kinetic energy $\hbar^2/2m|\mathbf{k}+\mathbf{G}|^2$ are usually more important (because of 1/k behavior of the Coulomb interaction) than with a large kinetic energy. The plane-wave basis set can therefore be truncated. In the process an error is made. When selecting a potential (pseudopotential, PAW, etc.) , it is necessary that with the selected cut-off energy the total energies of the system are converged when compared to the larger cut-off energies.

The Bloch's theorem cannot be applied to a system with a defect. Calculations with the plane-waves can only performed if a periodic supercell is used. A

supercell contains a defect with enough bulk around it to remove defect-defect interactions between neighboring cells. This requires, of course, a set of test calculations. The supercell is reproduced to fill the space to infinity [55].

2.2.4 Pseudopotential Approximation

The pseudopotential approximation makes use of the fact that the valence electrons are more important in determining the physical properties of a solid than the core electrons. In practise, this means that the Z/r behaviour of the core electrons is replaced by a weaker pseudopotential, which acts on a set of pseudowave functions rather than true valence wave functions (see Figure 2.3). The rapid oscillation of the valence wave functions in the region occupied by the core electrons due to the strong ionic potential maintain the orthogonality between the core and valence wave functions required by the exclusion principle. The construction of the pseudopotential is made so that its scattering properties or phase shifts for the pseudo wave functions are identical to the scattering properties of the ion and the core electrons for the valence wave functions in such a way that there are no radial nodes in the core region. In the core region, the total phase shift produced by the ion and the core electrons will be greater by π for each node the valence functions had in the core region than the phase shift produced by the ion and the valence electrons. Outside the core region the two potentials are identical, and the scattering from the two potentials is indistinguishable. The phase shift produced by the ion core is different for each angular momentum component of the valence wave function and so the scattering from the pseudopotential must be angular momentum dependent. The most general form for a pseudopotential is then

$$V_{NL} = \sum_{lm} |lm\rangle V_l \langle lm|, \tag{2.59}$$

where $|lm\rangle$ are the spherical harmonics and V_l is the pseudopotential for angular momentum l. This operator decomposes the electronic wave function into spherical harmonics and each of them is multiplied by pseudopotential V_l.

A pseudopotential that uses the same potential for all the angular momentum components of the wave function is called a local pseudopotential. In this case the pseudopotential is a function of the distance from the nucleus. It is possible to produce arbitrary, predetermined phase shifts, but there are limits to the amount that the phase shifts can be adjusted for the different angular momentum states, while maintaining the smoothness and weakness of the pseudopotential. The shortcoming of this approach is the difficulty in expanding the wave functions using a reasonable number of plane-wave basis states [55].

2.2.5 Projector Augmented-Wave Method

A basic strategy of the augmented-methods is to divide space into regions, i.e. to make a partial-wave expansion near atom-centered sphere and envelope functions outside the spheres. The basic formalism in the Projector Augmented Wave-Method [56] is the following: A definition for a linear transformation is

$$\tau = 1 + \sum_R \hat{\tau}_R \tag{2.60}$$

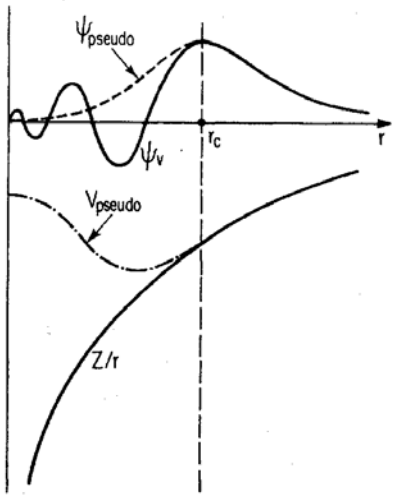

Figure 2.3: Schematic illustration of all-electron (solid lines) and pseudoelectron (dashed lines) potentials and wave functions. The radius at which all-electron and pseudoelectron values match is designated r_c. [55]

where $\hat{\tau}_R$ acts inside some augmentation region Ω_R enclosing the atom. $\hat{\tau}_R$ is defined for each augmentation region individually by specifying the target functions $|\phi_i\rangle$ for a set of initial functions $|\tilde{\phi}_i\rangle$, which are orthogonal to the core states and complete in Ω_R, i.e. $|\phi_i\rangle = 1+\hat{\tau}_R|\tilde{\phi}_i\rangle$. $|\phi_i\rangle$ are called all-electron (AE) partial waves and $|\tilde{\phi}_i\rangle$ pseudo (PS) partial wave functions. A natural choice for the AE partial waves are solutions of the radial Schrödinger equation for the isolated atom, which are orthogonalized if necessary. A connection between PS and AE waves is that they are equal outside the augmentation region.

Considering an all-electron wave function (a full one-electron Kohn-Sham wave function), which can be presented as

$$|\Psi\rangle = \tau|\tilde{\Psi}\rangle = \sum_i |\phi_i\rangle c_i, \text{ within } \Omega_R, \tag{2.61}$$

and a similar expression can be written for

$$|\tilde{\Psi}\rangle = \sum_i |\tilde{\phi}_i\rangle c_i, \text{ within } \Omega_R. \tag{2.62}$$

The requirement that the transformation τ to be linear guarantees that the coefficients are linear functionals of the PS wave functionals. Hence, the coefficients are scalar products

$$c_i = \langle \tilde{p}_i|\tilde{\Psi}\rangle, \tag{2.63}$$

where the functions $|\tilde{p}_i\rangle$ are called projector functions for each PS wave. The projector functions must fulfill the condition $\sum_i |\tilde{p}_i\rangle\langle\tilde{\phi}_i| = 1$ within Ω_R. This means that the one-center expansion $\sum_i |\tilde{p}_i\rangle\langle\tilde{\phi}_i|\tilde{\Psi}\rangle = |\tilde{\Psi}\rangle$.

In summary, Equations (2.61) and (2.63) define the linear transformation to be used. The three quantities, which are determined from this transformation are:

- the AE partial waves $|\phi_i\rangle$, obtained by radially integrating the Schrödinger equation of the atomic energy for a set of energies ε_i^1 and orthogonalization to the core states, i.e. the core state can be expressed as

$$|\Psi^c\rangle = |\tilde{\Psi}^c\rangle + |\phi^c\rangle - |\tilde{\phi}^c\rangle \tag{2.64}$$

- PS partial wave $|\tilde{\phi}_i\rangle$, which coincides with the corresponding AE partial wave outside some augmentation region for each AE partial wave

- one set of projector functions $|\tilde{p}_i\rangle$ for each PS partial wave localized within the augmentation region, and obeys the relation $\langle\tilde{p}_i|\tilde{\phi}_j\rangle = \delta_{ij}$.

The variational variable is $|\tilde{\Psi}\rangle$. The implementation of PAW-method into a pseudopotential code can be done with relative ease (and it is done in Ref. [57]). One benefit of the PAW method is that it takes in a sense the core electrons into account. The core region is well established. The approximation, which is made in both pseudopotential and PAW calculations, is freezing the cores. In the search of energy minimum, modern computer algorithms can optimize the position of ions using the Hellmann-Feynman forces [58, 59].

2.3 VASP

In this thesis the Vienna Ab Initio Simulation Package (VASP) is used as the main work horse. VASP is a package for calculating ab-initio quantum-mechanical simulations using pseudo-potentials (PP) or the PAW-method with the plane wave basis set. The execution time of parts of plane wave codes usually scales like N^3 where N is the number of electrons in the system. In VASP the prefactors before the cubical term are negligible, leading to an efficient scaling with respect to system size. This has been achieved by evaluating the non-local parts of the pseudo-potential in real space and by keeping the number of orthogonalisations at a minimum.

The implementation in VASP is based on the (finite temperature) LDA with the free energy as a variational quantity and an exact evaluation of the instantaneous electronic ground state at each MD step. VASP uses an efficient Pulay-Broyden charge density mixing. These techniques avoid all problems possibly occurring in the original Car–Parrinello method, which is based on the simultaneous integration of electronic and ionic equations of motion. The interaction between ions and electrons by ultra-soft Vanderbildt pseudo-potentials (US-PP) or by the PAW-method. These pseudo-potentials and the PAW method allow for a considerable reduction of the number of plane-waves per atom for transition metals and first row elements. Generally, not more than 100 plane waves per atom are required to describe the bulk properties of a solid. Forces and the full stress tensor can be calculated easily, and used to relax atoms into their instantaneous ground state.

The combination of self-consistency cycle to calculate the electronic ground state with efficient numerical methods has lead to an efficient scheme for evaluating the self-consistent solution of the Kohn-Sham functional. The implemented iterative matrix diagonalisation scheme is among the fastest available schemes.

The symmetry of an arbitrary configuration is automatically determined in VASP. The symmetry code is also used to set up the Monkhorst-Pack special

points allowing an efficient calculation of bulk materials and symmetric clusters. The integration of the band-structure energy over the Brillouin zone is performed with smearing or tetrahedron methods [60, 61, 62].

Chapter 3

Magnetic Properties of Frenkel Pairsin Graphene

3.1 Introduction

There are two main types of intrinsic defects: vacancies and interstitials, and dislocations. Vacancy means that one ion is missing and interstitial that there is an extra ion in the crystal. These defects are usually the cause for the observed conductivity of ionic crystals, and they have a significant effect on the optical properties (especially on the color). They are always present in thermal equilibrium, which makes them intrinsic in nature [53]. Dislocations are line defects, and they do not have thermodynamic origin. Instead, dislocations are caused by stresses affecting a sample during growth. Dislocations are essential in explaining the observed strength (or lack of it) of real crystals and the observed growth rates [53]. Since recombination of proximate Frenkel partners is very probable, in this section the properties of isolated adatoms and vacancies in carbon systems are considered - specifically a graphene sheet and various nanotubes.

Besides vacancies and interstitials, there are other types of simple defects, such as Stone-Wales defects (two heptagons and two pentagons), formed by rotating a carbon-carbon bond by 90 degrees [63]. The barrier for such defect formation is lower than that for Frenkel pairs, especially if an extra carbon atom, which works as a catalyst is nearby [64]. However, this defect is nonmagnetic, so it is not considered further.

The abundance of open space in nanotubes suggests that the interstitial atom can also be treated as an *adatom* adsorbed onto the nanotube surface [65, 66]. This is particularly the case for isolated single-walled nanotubes (SWNT) and interstitials in the inner cores of the tubes. However, the nature of the vacancies and interstitials in graphite and multi-walled nanotubes (MWNT) is complicated by the presence of nearby layers. If graphite is considered as an example, it is clear that the properties of vacancies and interstitials may be affected by the presence of the second layer. However, as discussed in the previous section, any treatment of interlayer processes with DFT ignores the fact that the van der Waals interaction between layers is incorrectly represented. Hence, it is probably better, and still qualitatively correct, to consider only a

single graphene sheet as a good model of graphite.

3.2 Properties of Adatom on Graphene

3.2.1 Equilibrium Position

The first *ab initio* calculations concerning the properties of an adatom on a single sheet of graphite (graphene) were performed by Mattila and coworkers [67] in the middle of 1990s. Using a 50-atom size sheet and LDA the authors of that work concluded that the ground state of an adatom was in a bridge-like structure.

The development of computing techniques and computers alongside the renewed interest on the carbon materials made it tempting to recalculate the ground state properties of the carbon atom on a sheet of graphite. Using GGA with the full relaxation of the spin produced a whole set of results [68]: The adatom is 1.87 Å above the surface (2.0 Å in Mattila's studies), the distance to the adatom's nearest neighbors is 1.52 Å and the distance between the nearest neighbors is 1.58 Å. The adsorption energy was found to be 1.40 eV (3.30 eV in Mattila's studies and 1.2 eV in Heggie's work [69], and 1.78 eV in Lee's work [70]). A new property of the equilibrium position of adatom was that the ground state has a magnetic moment of 0.45 μ_B. The magnetism arises from the interaction between the sp^2- and unhybridized p_x-orbital, which transfers charge from the p_x-orbital to the dangling sp^2-orbital (see Figure 3.1 [68]). The orbital-orbital interaction, which is the cause of the adatom's magnetism,

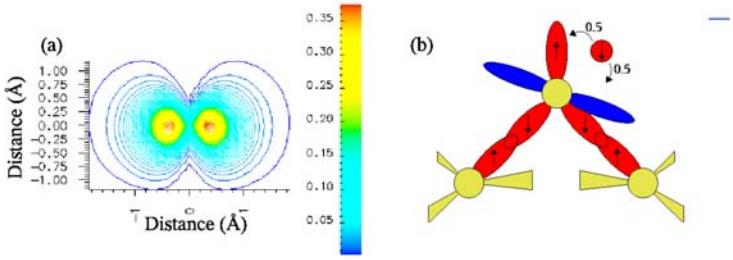

Figure 3.1: (a) Spin density in e/Å^3 of plane normal to surface through center of adatom when adatom is at equilibrium position. The adatom is at (0,0). (b) A Schematic diagram of bond orbitals at the equilibrium position in a plane through the adatom and two surface carbons. Note that this schematic is a projection, and that the blue p-orbital is orthogonal to the adatom-surface bonds.[68]

is caused by the breakdown of the symmetry of the sp^2-hybridization. In the graphene plane, the angle between each bond is 120°. When three carbon atoms form a bridge structure, it is obvious that the angles differ from 120°.

3.2.2 Migration of Adatom

The study of the migration path is crucial in determining the dynamics of the defect. The migration energy path gives two important pieces of information:

The migration energy barrier tells how stable the defect is, i.e. how easily defect's properties can be measured, and the path provides information about what happens to the magnetism during the motion of the defect.

The calculated migration path of an adatom is almost a straight line (see Figure 3.2). During the migration between the equilibrium positions, the magnetic moment disappears because the adatom's hybridization changes from sp^2- to sp-like (only one bond attached to the surface) leaving one dangling bond, p_x-, and p_y-orbitals free. The p-orbitals then interact with themselves creating π-orbitals, which interact then with the remaining sp-orbital. The result is much more delocalized density and the magnetism is destroyed. The migration energy barrier is 0.47 eV (Figure 3.3) (0.1 eV in Heggie's work [69]). These facts mean that the adatom is highly mobile on the plane at room temperatures, and experimental observation is difficult. The diffusion through the layers has an energy barrier of 2.3 eV [71] making in-plane motion of an adatom favorable.

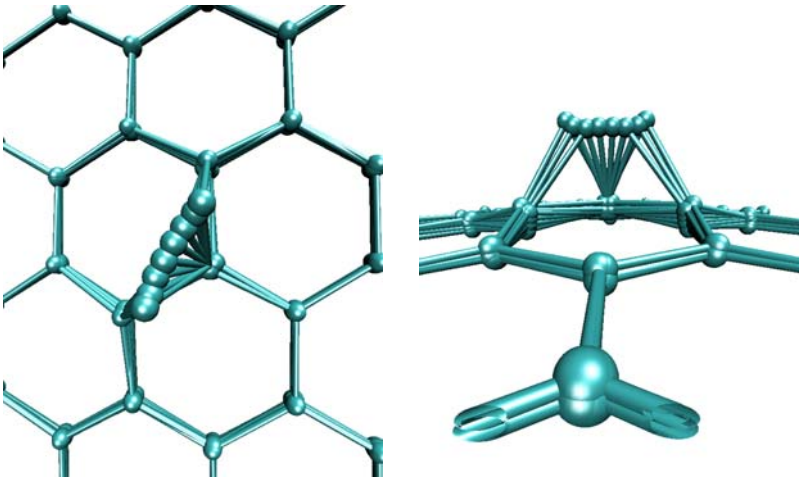

(a) (b)

Figure 3.2: Migration path of adatom on graphene from (a) top and (b) side. The starting point of the path is the equilibrium position and the end point is another equilibrium position. They are both so-called bridge-like structures. The middle points of the path, where adatom has two bonds, is actually a transition point from magnetic to non-magnetic situation. The reason is the change in the hybridisation of the adatom.

3.3 Clustering of Adatoms

Since it is known that adatoms are very mobile, an obvious question is whether they form clusters on the surface. The clusters have properties depending on their size, as will be shown. The smallest clusters, dimers and trimers, are studied here.

The adsorption energy of a carbon atom above another carbon atom forming

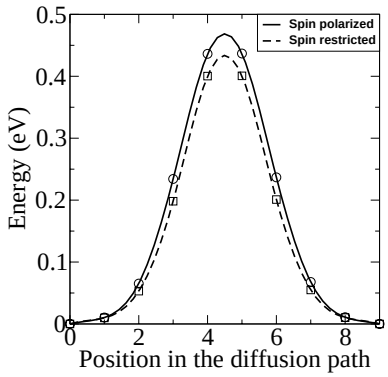

Figure 3.3: Migration energy barrier of adatom on graphene.[68]

the top of a bridge structure, as shown in Figure 3.4(a), is 8.7 eV. This system is not magnetic since the the dangling sp^2-bond of the bridge forms a bond with the sp-orbital of the upper carbon ion. The p_x-orbital of the carbon ion at the bridge configuration interacts with the p-orbitals of the upper carbon ion becoming π-orbital as in graphene. The reason why the sp-type dangling bond does not have a magnetic moment is as in the case of an adatom alone.

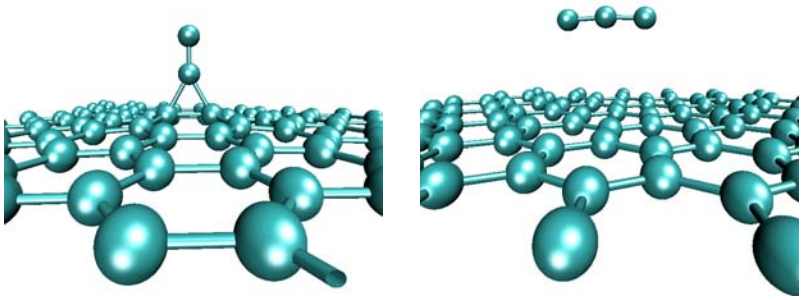

(a) (b)

Figure 3.4: Clustering of multiple adatoms. The equilibrium structure of two adatoms (dimer) in Fig. 3.4(a) and three adatoms (trimer) in Fig. 3.4(b).

Making a similar calculation with a carbon trimer results in a linear C-C-C equilibrium configuration parallel to the surface plane. Compared to the perfect graphene sheet and three isolated carbon atoms this structure has 12.2 eV lower energy, demonstrating that adatoms will cluster on the surface. In contrast to the dimer, the trimer is magnetic, but with a lower moment than the adatom (0.2 μ_B). Since C-C-C is composed of sp-bonds, the conclusion is that the dangling sp-bonds interact first with the p-orbitals preventing the formation of π-orbitals. In general, these results suggest that all clusters with an even number of atoms will be non-magnetic, and all odd will be magnetic - but the moment decays rapidly with the size of the cluster. However, any quantitative conclusions would require an extensive study of cluster growth and include the

effects of interlayer interactions.

3.4 Properties of Adatom on Nanotubes

3.4.1 Ground State Properties

Because the structure and bonding in carbon nanotubes are very similar to that of graphite, it is interesting to explore whether adatoms are also magnetic on nanotubes. The ground state of an adatom on nanotubes is in a bridge-like structure as in graphite. There are slight differences in bridge-structures depending on the position of the bridge and depending on a tube. Figures 3.5 and 3.6 show the equilibrium positions of an adatom on zigzag and armchair nanotubes, respectively. The parallel position (the bridge is parallel to the translational axis of the tube) shown in Figures 3.5(a) and 3.6(a) is a metastable position, as can be seen in the Table 3.1 [72], while perpendicular position (the Figures 3.5(b) and 3.6(b)) is the ground state position. The small zigzag nanotubes are semi-

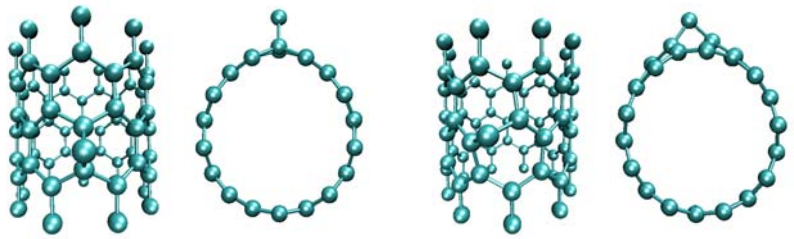

(a) (b)

Figure 3.5: Equilibrium positions of adatom on (9,0) nanotube in (a) parallel and (b) perpendicular positions.

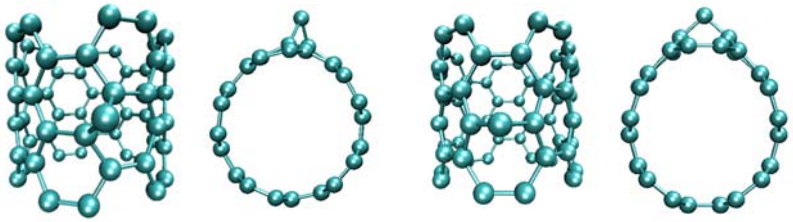

(a) (b)

Figure 3.6: Equilibrium positions of adatom on (5,5) nanotube in (a) parallel and (b) perpendicular positions.

conductors while the armchair nanotubes are always metals. This difference in the electronic structure has an effect on the magnetic moment of an adatom. There are three factors to be considered when evaluating the magnetic moment

Table 3.1: Data for various nanotubes considered in this study. [72].

Nanotube	Class	Radius (Å)	Adsorption Energy (eV)		Magnetic moment (μ_B)	
			Par.	Perp.	Par.	Perp
(8,0)	Semiconducting	3.13	2.37	2.89	0.01	0.23
(10,0)	Semiconducting	3.96	2.09	2.57	0.25	0.23
(11,0)	Semiconducting	4.41	2.03	2.49	0.20	0.22
(5,5)	Metallic	3.39	2.33	3.29	0.23	0.44
(9,0)	Semiconducting	3.57	2.35	2.80	0.24	0.35
(6,6)	Metallic	4.07	2.15	2.91	0.27	0.43
(12,0)	Semiconducting	4.97	2.04	2.50	0.32	0.36
Graphene	Metallic	∞	1.40	1.40	0.45	0.45

of an adatom: the electronic structure of the tube, the location of the bridge on the tube, and the radius of the tube itself. If a nanotube, on which an adatom lies, is semiconducting, some of the adatom's charge goes to decreasing the band gap of the tube. If the gap is small enough, the defected tube becomes metallic, which is what happens with (9,0) and (12,0) nanotubes. This change in electronic structure takes place in the vicinity of the defect, so if the concentration of defects is low enough, the rest of nanotube remain semiconducting. If the adatom's unhybridized p-orbital is parallel to the translational axis of the tube as in Figure 3.6(b), the situation is very close to graphene since the curvature of the tube in this direction is the same as graphene's, namely infinite. When an adatom is on a zigzag nanotube at the parallel position (see Figure 3.5(a)), the p-orbital is perpendicular to the translational axis of the tube. If the tube's radius is small enough, as for example in (8,0), the p-orbital interacts with itself around the tube destroying the moment. Thus, the size of the magnetic moment contributed by an adatom depends on the radius of the tube, which affects directly and indirectly, simultaneously.

3.4.2 Migration of Adatom on Nanotubes

Migration of adatoms on nanotubes is important because this issue is directly related to the stability of magnetic defects. Also, the effects of the curvature and varying electronic structure on the migration barrier of an adatom will be studied.

In order to study migration of adatoms on nanotubes, two complementary approaches have been used. First, standard PW-DFT to calculate the adsorption energies for several different nanotubes, and to find the migration path and barrier for one tube. Using this as a reference, the accuracy of the computationally cheaper DFT-TB method is tested. Figure 3.7 shows the comparison of adsorption energies, and demonstrates good qualitative agreement - note that the PW-DFT results differ from the DFT-TB (using LDA) by a constant, which matches the difference between LDA and GGA in adsorption energies. Figure 3.8 also shows that the migration barrier is also in good agreement, hence DFT-TB is used to calculate the migration for a large number of tubes. Figure 3.8 shows the barrier as a function of radius for the armchair and zigzag tubes considered. As expected, the barrier decreases with increasing radius, and tends towards the limit of infinite radius, i.e. graphene.

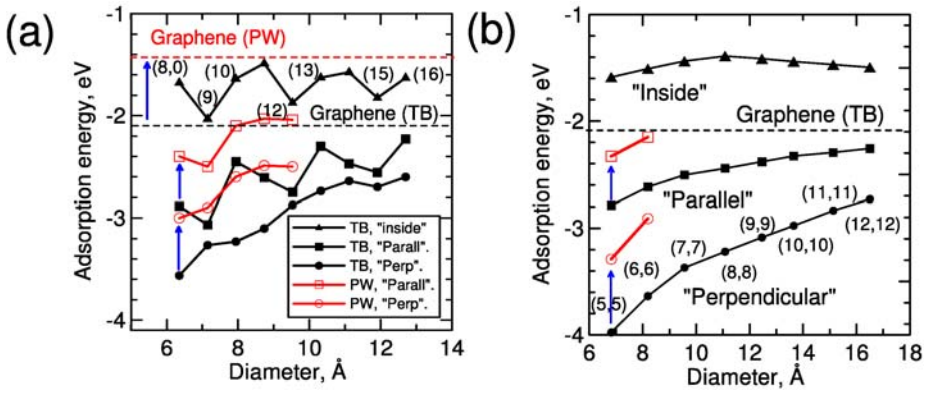

Figure 3.7: Adsorption energies of carbon adatoms on zigzag (a) and armchair (b) single walled nanotubes as function of nanotube diameter. The arrows visualize the relationships between the corresponding TB and PW results. The numbers stand for the tube chirality indices. [73]

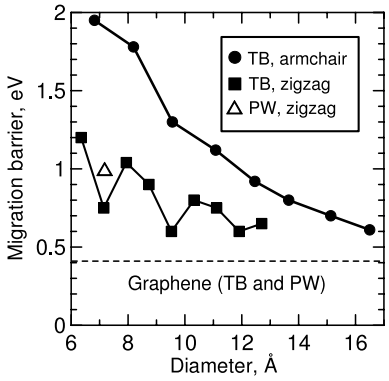

Figure 3.8: Energy barrier for adatom migration on the outer surface on nanotubes as function of nanotube diameters. Here the graphene migration barrier is the same for the PW and TB calculations. [73]

3.5 Vacancy in Graphene

In order to remove a carbon ion from the carbon network, of which the graphene is composed, 7.7 eV (calculated as in Ref. [74]) is needed in agreement with previous DFT results of 7.6 eV [75] and 7.4 eV [76]. Atoms 1 and 2 (see Figure 3.9) form a bond creating a pentagon. The distance between atoms 1 and 2 is 2.02 Å compared to the 1.42 Å in graphene. Atom 3 is elevated from the surface through the Jahn-Teller displacement of about 0.18 Å (0.47 Å and no magnetism in Ref. [76]). The vacancy is magnetic with a magnetic moment of 1.04 μ_B. The explanation is as follows: The removal of one carbon ion creates three unsaturated sp^2-orbitals in the neighboring carbon ions. The formation of the pentagon saturates two of them, which leaves one sp^2-orbital free. This remaining dangling bond contributes the calculated magnetic moment as can be seen in Figure 3.10.

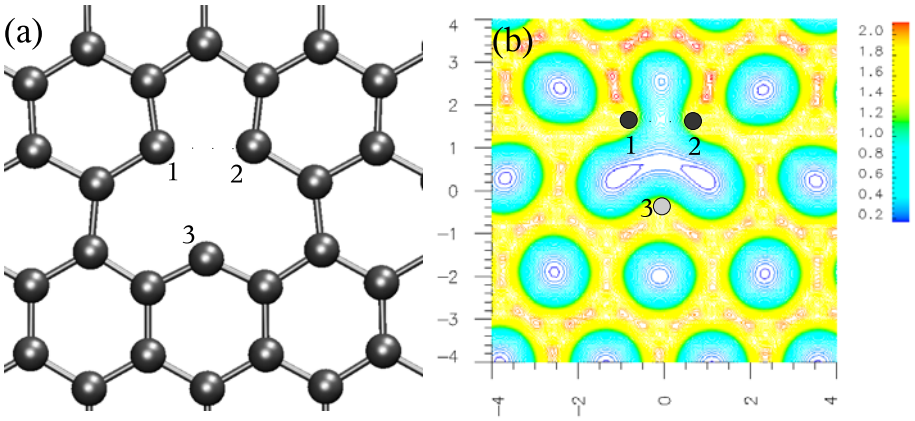

Figure 3.9: (a) Atomic structure of vacancy in graphene plane. (b) The charge density of a vacancy in the graphene plane (e/Å^3). [77]

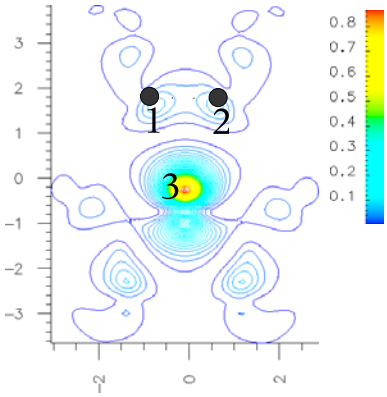

Figure 3.10: Spin density of vacancy in graphene plane (e/Å^3). [77]

3.5.1 Migration of Vacancy in Graphene

The calculated migration energy barrier of a vacancy is 1.41 eV (see Figure 3.12), which is in agreement with 1.7 eV in Ref. [78] and with previous studies [79, 80], but in disagreement with the experimental value of 3.1±0.2 [81]. Such a clear disagreement between the experiments and theory suggests that experiments have failed to measure the migration energy of a single vacancy, and instead the migration of divacancy is measured. Thus, it is clear that the interstitials move faster than the vacancies in graphite. The inter-plane migration of a vacancy is a much more difficult with the experimental migration barrier of more than 5 eV [81]. Thus, in-plane migration is favourable for both types of defects.

The migration path of a vacancy is shown in Figure 3.11 and the corresponding migration energy barrier in Figure 3.12. A bond rotation occurs between points 10-12 which costs 0.2 eV in agreement with calculations in Ref. [76]. Points #3, #4, #6, #7 and #9 do not carry a net magnetic moment. The main difference between points #4 and #5, and on the other hand points #8 and #9, is the bond length of the pentagon bond. In the non-magnetic cases it is 2.00 Å(#4) or 1.98 Å(#9) while in the magnetic cases the length of the pentagon bond is 1.87 Å(#5 and #8). The reason for this magnetic moment is in the formation process of a bond, which seems to start with spin-polarization of the sp^2-orbital.

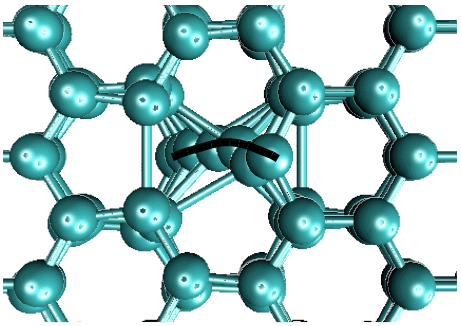

Figure 3.11: Migration path of vacancy in graphene.

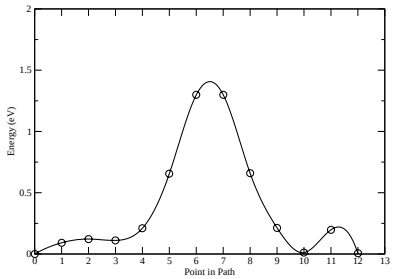

Figure 3.12: Migration energy barrier of vacancy in graphene.

Table 3.2: Properties of 5-ring armchair SWNTs with vacancies of different configurations. [77]

Nanotube	Configuration	E_{for} (eV)	Class	Mag. (μ_B)
(3, 3)	Perp.	4.4	Semi.	0.0
	Par.	5.2	Metal	1.0
(4, 4)	Perp.	5.3	Semi.	0.0
	Par.	6.2	Metal	1.0
(5, 5)	Perp.	5.6	Metal	0.6
	Par.	7.1	Semi.	0.0
(6, 6)	Perp.	5.9	Semi. (Metal[1])	0.0 (0.4[1])
	Par.	7.3	Semi.	0.0

[1] 4-ring (6, 6) tube.

3.6 Vacancy in Nanotubes

The description of magnetic properties of a vacancy in nanotubes is much more difficult task. The properties of a vacancy in a nanotube are due to an interplay of the following facts: first, nanotubes are cylinders, not flat planes. The ions guarantee that a nanotube is a three dimensional object. The surroundings of a vacancy may have more than one configuration, and all of them need to be checked in order to find the ground state. Secondly, the size of the tube changes when the chirality vector changes. This has an implication that a ground state vacancy configuration may not be a general ground state for all tubes regardless of the chirality. Thirdly, in nanotubes the electronic structure varies in perfect zigzag nanotubes between semiconducting and metallic, and the perfect armchair nanotubes are always metallic. The electronic structure changes easily when there are defects in the system. These facts mean a large set of calculations, and the calculated results for different configurations (see Figures 3.13(a) and 3.13(b) [77]) are collected in Tables 3.2 and 3.3.

The configuration shown in Figure 3.13(c) has the following properties: Each carbon ion is sp^2-hybridized. The carbon atom with a dangling bond has magnetic moment of 1 μ_B and creates a metallic band. This metallic band is created by the redistribution of the charge within the hexagonal carbon network of the nanotube. In this sense, the behavior is similar to the behavior of an adatom on a nanotube. However, the magnetic properties of a nanotube with a vacancy depend much more on the curvature of the tube than the properties of a nanotube with an adatom because with a smaller tube the effect of removal of an atom is larger. If the Jahn-Teller effect seems to be of similar size in absolute scale, this means that the Jahn-Teller effect is much larger in smaller nanotubes in relative scale. The reason for larger Jahn-Teller effect in smaller tubes is the stress inherent in every nanotube, and in smaller nanotubes the stress is always stronger than in larger nanotubes.

Figure 3.13(a) shows the ground state of the vacancies for (5,5) and (6,6) nanotubes. The (5,5) nanotube with a vacancy at the perpendicular configuration is magnetic because the Jahn-Teller distortion is large-enough to form the bridge structure (although not sufficient to get 1 μ_B). The relaxations of

Table 3.3: Properties of 6-ring zigzag SWNTs with vacancies of different configurations. [77]

Nanotube	Configuration	E_{for} (eV)	Class	Mag. (μ_B)
(5, 0)[1]	Perp.	4.6	Semi.	0.0
	Par.	5.1	Semi.	0.0[2]
	3db	6.0	Semi.	0.0[2]
(6, 0)	Perp.	5.0	Metal	0.3
	Par.	5.8	Metal	0.9
(7, 0)	Perp.	5.2	Semi.	0.0
	Par.	6.3	Metal	0.8
(8, 0)	Perp.	5.3	Semi.	0.0
	Par.	6.5	Metal	0.8
(9, 0)	Perp.	5.4	Semi.	0.0
	Par.	6.4	Metal	1.0
(10, 0)	Perp.	5.5	Semi.	0.0
	Par.	6.7	Metal	0.9
	3db	7.4	Metal	1.9

[1] 8-ring (5, 0) tube.

[2] Anti-ferromagnetic.

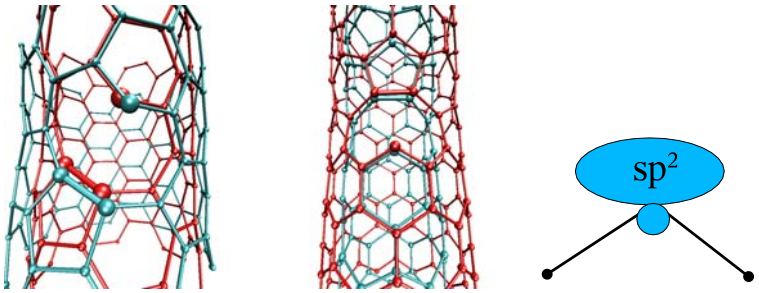

(a) (b) (c)

Figure 3.13: Ground state of vacancies in zigzag and armchair nanotubes. In Fig. (a) are (5,5) (red) and (6,6) (opaque) armchair nanotubes and in Fig. (b) are (6,0) (opaque) and (9,0) (red) nanotubes. Although the nanotubes are shown inside each other they were calculated separately. In Fig. (c) calculated properties of tubes with a vacancy follow from the properties of this configuration.

the rest of the tube are small enough so that the overall electronic structure remains metallic. For the (6,6) nanotube, the Jahn-Teller effect is dependent on the linear density of the vacancies along the tube. It is not large enough for a magnetic ground state if the density is less than 1 vacancy per 4 carbon rings. The smaller radii (3,3) and (4,4) armchair nanotubes demonstrate perfectly the bridge configuration, giving a magnetic moment of 1 μ_B in the parallel position.

The bridge configuration is also responsible for the magnetism and metallic electronic structure of the parallel vacancy in larger zigzag-tubes such as (7,0), (8,0), (9,0) and (10,0) (see Fig. 3.13(b)). When the vacancy is in the perpendicular configuration, these tubes remain semiconductors, as the removal of the ion increases the gap. The ideal (6,0) nanotube is metal, and no matter where the vacancy is located, it remains metallic and has a magnetic moment. (5,0) is a semiconductor due to an extensive damage on the networks caused by the vacancy on a small tube, preventing the formation of a metallic band.

The question as to what happens with an open ended nanotube was studied in Ref. [23]. If the other end of a nanotube is capped with a fullerene, the authors found that the edge atoms have a magnetic moment of 1.25 μ_B per dangling bond. If a nanotube has both edges open, the spins of the dangling bonds are antiferromagnetically ordered. If the dangling bonds at one edge are saturated with hydrogen, the spins in the open edge contribute most to the total magnetic moment ($1\mu_B$ per atom). In the (8,0) nanotube the authors found a small polarization of p-orbitals at carbons attached to the hydrogen atoms at the edge. The magnetic state generated by vacancies, zigzag edges at nanotube ends, and defective fullerenes are very similar, and point very clearly to the flatband mechanism of magnetism already studied in Refs. [20, 82].

Chapter 4

Magnetism Stimulated by Non-Magnetic Impurities

In addition to creating intrinsic defects in carbon materials, ion irradiation may also lead to doping of the sample by the impinging ions. Specifically, the irradiation of graphite by protons has been shown experimentally to induce a significant magnetic signal [29]. Since similar irradiation by helium ions produces a much weaker signal, it cannot be simply explained by the generation of vacancies and adatoms. Hence, the properties of hydrogen and helium in graphite via DFT-GGA simulations are considered, and whether they a play role in the observed magnetism examined.

The adsorption energy of H on perfect graphene is 0.87 eV (0.71 eV in Ref.[83], 0.76 eV in Ref. [84], 0.76 eV in Ref. [85] and 0.67 eV in Ref. [86]) and the adsorption position is above another carbon ion. This configuration has no magnetic moment unless the density of hydrogen on the surface is very high, i.e. approaching a few percent [85]. In any case, above a graphene sheet the hydrogen is quite mobile (barrier 1.30 eV for an isolated H on graphene, but reducing to 0.48 eV near other H atoms [84]) and does not form a dimer easily since the barrier for recombination is 2.82 eV [84]. Hence, it is highly probable that hydrogen migrates on the plane until it is pinned by another defect.

If the hydrogen encounters an empty vacancy, it saturates the dangling bond, and is pinned at a height of 1.25 Å above the plane (Figure 4.1), with an adsorption energy of 4.36 eV. This configuration is non-magnetic. This result contrasts with studies of the effect of a hydrogen on a vacancy-like defect in fullerenes [27], where a magnetic moment of 3.0 μ_B per C_{60}-cage was observed. However, the local structure in the fullerenes is different, and the under-coordinated carbons cannot saturate bonds with each other due to the increased strain in the system. Hence, hydrogen saturates only one dangling bond and the local moment is provided by the other two sites. In the context of hydrogen migration through a layer, a similar configuration can be considered in graphene (see Figure 4.2), where hydrogen adsorbs directly into the vacancy, in-plane with the graphene sheet. The calculated migration path of a hydrogen through the graphite vacancy is shown in Figure 4.3, and the migration barrier is 1.25 eV. In points #1, #2, #3, #4 and #5 a pentagon bond is formed, and the rest of the points are in the process where hydrogen raises out of the plane. The saddle point (#0) is at

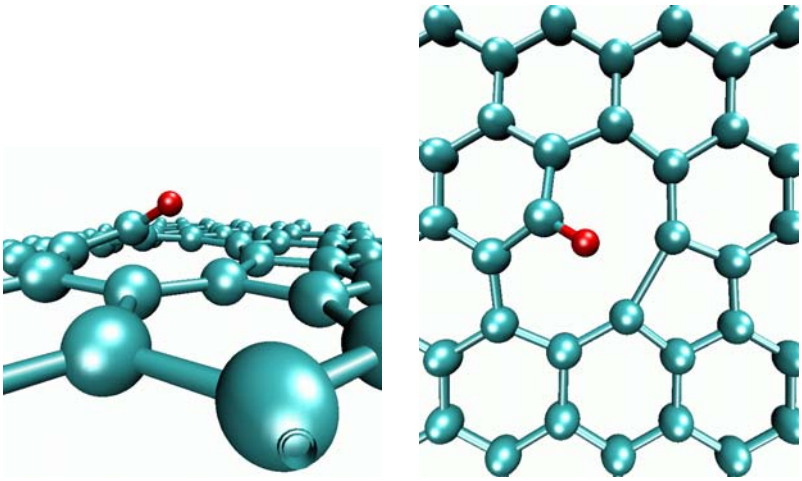

(a) (b)

Figure 4.1: Ground state of hydrogen in graphite vacancy.

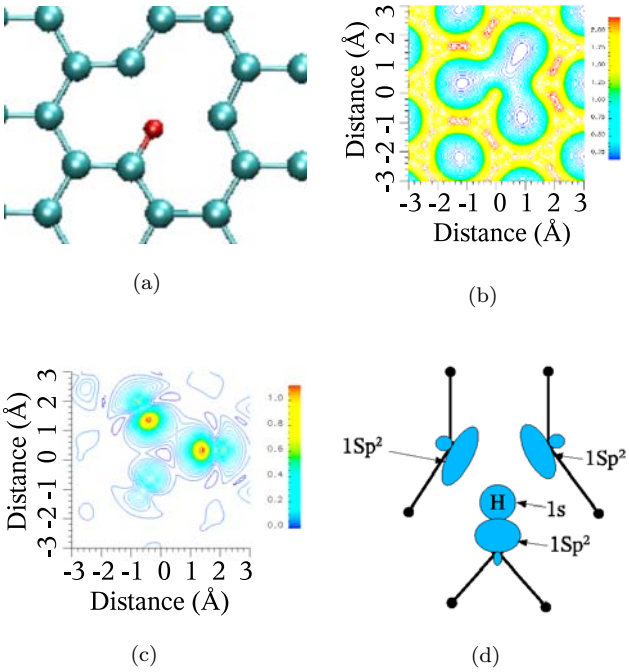

(a) (b)

(c) (d)

Figure 4.2: Saddle point of hydrogen migrating through vacancy: (a) atomic structure geometry, (b) charge density in plane of graphene sheet centered on hydrogen (eV/Å), (c) spin-density and (d)simple model explaining calculated magnetism.

the graphite plane. This position of a hydrogen is magnetic. The reason is that the hydrogen forces the ions forming the base of pentagon to move away from each other (Fig. 4.2(a)). From the basis of Figure 4.2(b), which is the charge density of the vacancy site, it is certain that the pentagon bond is significantly weakened. The resulting magnetic moment is 2.3 μ_B, and the spin-density (Fig. 4.2(c)) shows that this is mainly due to two dangling bonds on the separated carbon. With the help of a simple model figure (Fig. 4.2(d)) the interpretation of the result is the following: The hydrogen's 1s and one of the dangling bonds form a bond. The electron cloud around the hydrogen atom becomes thinner and it attracts the electrons localized in the dangling bonds of the other nearest neighbor carbon atoms. Hence, the sp^2-orbitals are directed toward the hydrogen ion and do not bond with each other. These two dangling bonds contribute a magnetic moment of 2 μ_B. Now the remaining magnetic moment comes from the 1s-sp^2 bond. Since 1s is spherical, not all of its charge is committed to the bond; only half an electron is contributed to the bond making- but suppressing the magnetism of the sp^2-bond a whole electron is required. Hence 1s-sp^2 bond becomes magnetic and contributes a magnetic moment of 0.5 μ_B. Since the method used cannot describe the van der Waals interactions properly, it is possible that in a multi-layered system this state becomes a deep metastable position, but other configurations seem more likely.

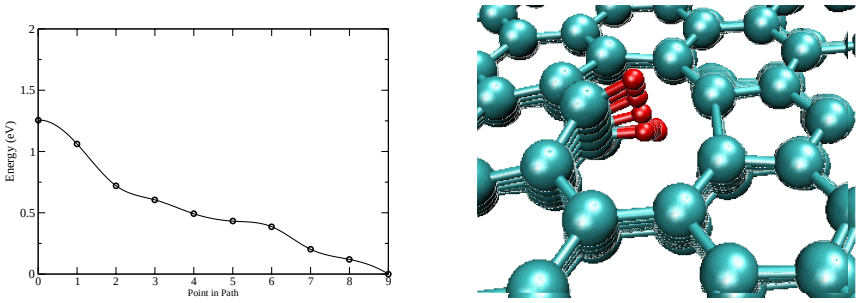

(a) (b)

Figure 4.3: Migration (a) barrier and (b) path of hydrogen through graphite vacancy.

Two stable magnetic configurations involving hydrogen do exist in graphite. Firstly, if a hydrogen atom encounters a vacancy which has already been saturated by hydrogen, it will bond to the other side of the vacancy (see Fig. 4.4(a)) with an adsorption energy of 3.2 eV, at a distance of 0.76 Å below the plane - the original H moves to 0.89 Å above the plane. This configuration has a magnetic moment of 1.2 μ_B localized on the dangling sp^2-bond (see Fig. 4.4(b)). Addition of a third hydrogen completes the decoration of the vacancy edges, saturates the remaining dangling bond, and thus destroys the magnetism of the vacancy. Adsorption energy to a system already occupied by two hydrogens is 4.0 eV.

If a hydrogen atom is pinned by an interstitial as shown in Figure 4.6, the

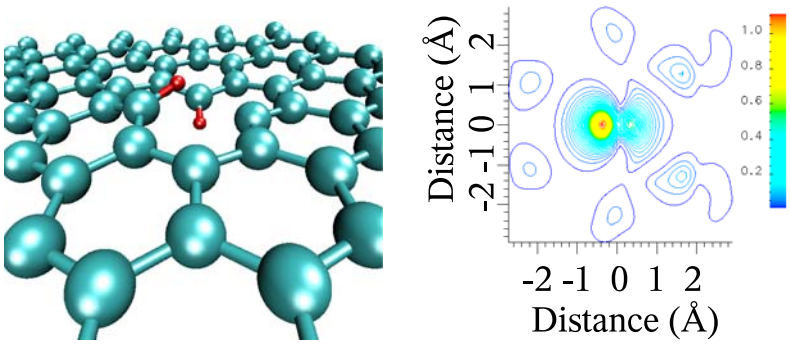

(a) (b)

Figure 4.4: Vacancy surrounded by two hydrogens. Figure (a) is the geometry and Figure (b) is the spin-density. The units are in $\mu_B/\text{Å}^2$.

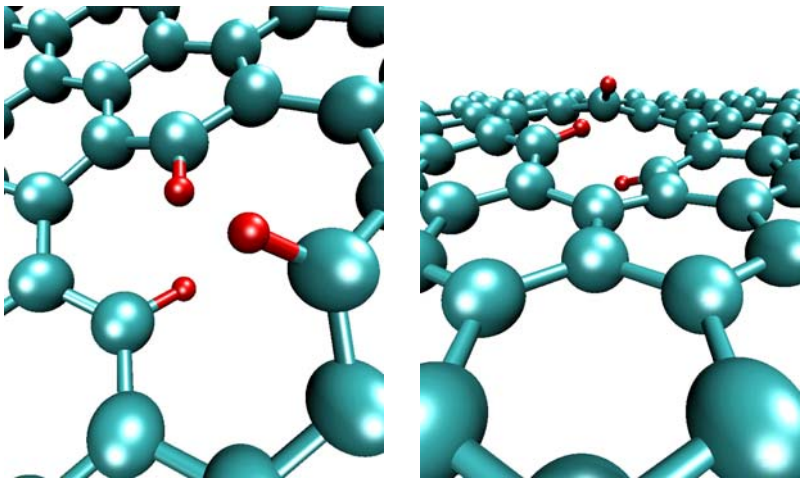

(a) (b)

Figure 4.5: Equilibrium structure of graphene vacancy and three hydrogen atoms.

adsorption energy is 5.0 eV. The second layer is added to see whether a bridge between the layers would form because of the C-H complex. Obviously, that is not the case. Instead, there is a deformation in the second layer and the C-H bond is tilted. The magnetic moment is 0.9 μ_B arising from the dangling sp^3-orbital.

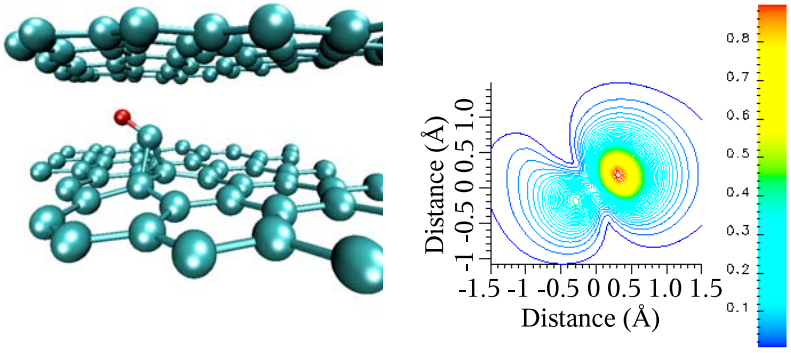

(a) (b)

Figure 4.6: (a) Ground state of hydrogen pinned by interstitial and (b) spin-density of CH group adsorbed between two layers of graphene.

Assuming that every hydrogen atom introduced by proton irradiation eventually will saturate a carbon dangling bond, then an estimation of the measurable magnetic signal can be made. Two hydrogen atoms at a vacancy result in a moment of 1.2 μ_B, and an adatom-hydrogen group provides a moment of 0.9 μ_B from the C-H itself, and 1.0 μ_B from the uncompensated vacancy. Hence, we can consider each hydrogen as providing an average moment of 1.25 μ_B. For an experimental dose of 3 μC (cf. Fig. 2 in Ref. [29]) of protons we get a signal of 0.2 μemu which is in an agreement with the experimental signal of 0.3 $\pm$ 0.2 μemu, and with higher dose of 10 μC the predicted signal is 0.8 μemu in agreement with 1 μemu. Obviously, it is very difficult to specify exactly the ratio of different defects that would actually be present in the irradiated material, but the agreement with the experimental magnetic signal strongly suggests that the H-vacancy complex plays a dominant role.

Irradiating graphite with helium produced quite different results [29] compared to the irradiation experiments with hydrogen, i.e. very small magnetic signal was observed. According to the calculations, helium has a ground-state well above the graphene sheet, and the interaction between graphite and helium is very weak. When the helium is in the ground-state it does not affect the magnetic signal created by the vacancy. If the helium is at the vacancy, then the magnetic signal is destroyed, but this situation is highly improbable. The conclusion is that helium creates initial defects, vacancies and interstitials, which migrate and some of them recombine, and some of them form interlayer

links resulting in magnetism close to zero.

Demonstration of magnetic ordering of the H-vacancy complexes due to the defect-defect interactions from the DFT calculations is difficult. For adsorbed hydrogen there are results, which indicate that the coupling on graphite is long ranged, even up to 25 lattice constants [87].

Thus, hydrogen contributes to the development of the macroscopic magnetic state in several different ways. Firstly, some defect configurations formed by vacancies and H atoms are magnetic. Secondly, hydrogen prevents complete recombination of Frenkel pairs, which should increase the number of intrinsic defects (without H). And finally, H atoms appear to favour the development of the long-range magnetic order.

Chapter 5

Conclusions and Outlook

In the Introduction, the most important problems of magnetism in carbon system are outlined. Theoretical findings, which shed light on two of the problems are summarized, and a partial answer is considered to the third question concerning different allotropes. Specifically, the local bonding geometry, which gives rise to local magnetic moments and the role of non-magnetic impurity atoms such as hydrogen, is addressed. The results presented in this thesis, along with those obtained by other authors, provide strong evidence for defect-mediated mechanism of magnetism in carbon systems, although contributions from other mechanisms cannot be excluded in some systems, e.g. carbon foams.

Adatoms and vacancies on a graphene sheet provide a localized magnetic moment - about 0.5 μ_B and 1.0 μ_B, respectively. In practice, however, the high mobility of adatoms on graphene at room temperature would suggest that many of them recombine with vacancies or cluster together, destroying their magnetism. Despite the indications that a barrier to vacancy-interstitial pair recombination exists [88], efficient recombination seems to be confirmed by He-irradiation experiments [29]. It is very well known that a large amount of point defects were produced by He ions, yet the magnetic signal was small.

For nanotubes the situation is even more complicated than in graphite. The surface curvature provides an increase in the adatom migration barrier, and hence, should increase the probability of stable magnetic defects, but the dependence of nanotube electronic structure on chirality affects the picture. Only for adatoms on armchair nanotubes is the defect picture similar to graphene, and both adatoms and vacancies on many other nanotubes are nonmagnetic. Some configurations provide a delocalized magnetic band, so, in principle, these would avoid issues of paramagnetism - but controlled production of nanotubes with a specific chirality is currently not possible.

The demonstration of induced ferromagnetism by proton irradiation on graphite [29] indicates a promising direction for creating a magnetic carbon system in a controllable way. Simulations indicate that this is due to a combination of hydrogen trapping at vacancies and pinning of mobile adatoms, producing magnetic C-H complexes and uncompensated vacancies. Hydrogen contributes to the development of the macroscopic magnetic state in several different ways. In addition to magnetic defect configurations formed by vacancies and H atoms, hydrogen prevents complete recombination of Frenkel pairs, which should increase the number of defects without H. Also, H atoms appear to favour the

development of long-range magnetic order.

The role of defects and non-magnetic impurities can be studied in more detail experimentally by irradiating the samples with energetic particles. To some extent, this has been already done previously [29]. However, systematic studies on irradiation of all-carbon systems with particles of different types and energies should give much more insight into the origin of magnetism. The irradiation temperature is also very important. For example, if carbon interstitials and vacancies can indeed contribute to magnetism, irradiation with electrons or inert gas ions at low (liquid helium or nitrogen) temperature followed by *in situ* magnetic measurements should detect a magnetic signal from the samples. By changing the temperature and thus annealing defects in the system one can, in principle, correlate magnetism to specific defect types, as different defects become mobile at different temperatures. Irradiation can also be used to introduce non-magnetic impurities like N or B atoms into the system, and aid in understanding the formation of the magnetic state.

Appendix A

Spatial Correlations in Fluids

Configurational distribution function is defined as (as in Ref. [89])

$$\int_V F_N(\mathbf{r}_1, \mathbf{r}_2, ..., \mathbf{r}_N) d^3r_1 d^3r_2 ... d^3r_N = 1. \tag{A.1}$$

After integration over $\mathbf{r}_1$ out and multiplying equaton (A.1) with N

$$F_1(\mathbf{r}_1) = N \int_V F_N(\mathbf{r}_2, \mathbf{r}_3, ..., \mathbf{r}_N) d^3r_2 d^3r_3 ... d^3r_N = n(\mathbf{r}_1), \tag{A.2}$$

which is the particle density an point $\mathbf{r}_1$. For homogenous systems F_1 is a constant which will be denoted as n. The two particle distribution function is now defined as

$$F_2 = N(N-1) \int_V F_N(\mathbf{r}_3, \mathbf{r}_4, ..., \mathbf{r}_N) d^3r_3 d^3r_4 ... d^3r_N = n^2 g(\mathbf{r}_2 - \mathbf{r}_1) = n^2 g(\mathbf{r}). \tag{A.3}$$

The product $g(\mathbf{r})d^3r$ determines the probablity of finding an another particle around the point $\mathbf{r}$ (or $\mathbf{r}_2$) when the other particle is in the origin (or at $\mathbf{r}_1$). For classical systems $g(\mathbf{r})$ is unity, and this is the reason why it is convenient to define

$$\nu(\mathbf{r}) = g(\mathbf{r}) - 1. \tag{A.4}$$

The next step is to consider the fluctuations of the number of the particles N_A occupying a region V_A. For this purpose one introduces a function

$$\mu(\mathbf{r}) = \begin{cases} 1 & \text{when } \mathbf{r} \text{ inside } \mathrm{V}_A \\ 0 & \text{when } \mathbf{r} \text{ outside } \mathrm{V}_A \end{cases} \tag{A.5}$$

and $N_A = \sum_i{}^N \mu_i$. The average value on N_A is given by

$$\begin{aligned} N_A =& \sum_{i=1}^{N} \int_V \mu(\mathbf{r}_i) F_N(\mathbf{r}_1, \mathbf{r}_2, ..., \mathbf{r}_N) d^{3N}r \\ =& N \int_V \mu(\mathbf{r}_1) d^3r_1 F_N(\mathbf{r}_1, \mathbf{r}_2, ..., \mathbf{r}_N) d^{3(N-1)}r \\ =& \int_V \mu(\mathbf{r}_1) F_1(\mathbf{r}_1) d^3r_1 = \int_{V_A} F_1(\mathbf{r}) d^3r = \int_{V_A} n(\mathbf{r}) d^3r, \end{aligned} \tag{A.6}$$

where the last equality comes from the fact that the system is homogeneous. The next step is to calculate the mean deviation:

$$\begin{aligned}
< N_A^2 > &= \sum_{i=1}^{N}\sum_{j=1}^{N} \int_V \mu(\mathbf{r}_i)\mu(\mathbf{r}_j) F_N(\mathbf{r}_1, \mathbf{r}_2, ..., \mathbf{r}_N) d^{3N} r \\
&= N_A + \sum_{i \neq j} \int_V \mu(\mathbf{r}_i)\mu(\mathbf{r}_j) F_N(\mathbf{r}_1, \mathbf{r}_2, ..., \mathbf{r}_N) d^{3N} r \\
&= N_A + N(N-1) \int_V \mu(\mathbf{r}_1)\mu(\mathbf{r}_2) d^3 r_1 d^3 r_2 F_N(\mathbf{r}_1, \mathbf{r}_2, ..., \mathbf{r}_N) d^{3(N-2)} r \\
&= N_A + \int_V \mu(\mathbf{r}_1)\mu(\mathbf{r}_2) d^3 r_1 d^3 r_2 F_2(\mathbf{r}_1, \mathbf{r}_2) \\
&= N_A + \int_{V_A} n(\mathbf{r}_1) n(\mathbf{r}_2) g(\mathbf{r}_1, \mathbf{r}_2) d^3 r_1 d^3 r_2 .
\end{aligned} \tag{A.7}$$

This means that

$$< N_A^2 > - N_A^2 = \int_{V_A} d^3 r n(\mathbf{r}) \{1 + \int_{V_A} d^3 r' n(\mathbf{r}') [g(\mathbf{r}, \mathbf{r}') - 1]\}. \tag{A.8}$$

If a derivative is taken with respect to the volume V_A and V_A' of Equation (A.8), and then divided with $n(\mathbf{r})$ the result is

$$\frac{< n^2 > - n^2}{n} = n(\mathbf{r}')[g(\mathbf{r}, \mathbf{r}') - 1] + \delta(\mathbf{r} - \mathbf{r}'). \tag{A.9}$$

Bibliography

[1] M. Winter, *http://www.webelements.com/* (2001).

[2] W. F. Coleman, *Hybrid Orbitals and the Localized Electron Model* (http://www.wellesley.edu/Chemistry/chem120/hybrids.html, 2003).

[3] R. Saito, G. Dresselhaus, and M. Dresselhaus, *Physical Properties of Carbon Nanotubes* (Imperial College Press, London, 1998).

[4] *A Rigorous Introduction to Graphite* (http://www.asbury.com/, Asbury Carbons).

[5] S. Iijima, Nature **354,** 56 (1991).

[6] M. Daenen, *Wondrous World of Carbon Nanotubes* (http://www.pa.msu.edu/cmp/csc/nanotube.html, 2003).

[7] M. Dresselhaus, G. Dresselhaus, P. Eklund, and R. Saito, *Carbon nanotubes* (http://physicsweb.org/article/world/11/1/9, 1998).

[8] N. Hamada, S. I. Sawada, and A.Oshiyama, Phys. Rev. Lett. **68,** 1579 (1992).

[9] J. W. Mintmire, B. I. Dunlap, and C. T. White, Phys. Rev. Lett. **68,** 631 (1992).

[10] M. S. Dresselhaus, G. Dresselhaus, and R. Saito, Phys. Rev. B **45,** 6234 (1992).

[11] O. Gülseren, T. Yildirim, and S. Ciraci, Phys. Rev. B **65,** 153405 (1992).

[12] Y. Kopelevich, P. Esquinazi, J. Torres, and S. Moehlecke, J. Low Temp. Phys. **119,** 691 (2000).

[13] T. Makarova, B. Sundqvist, R. Höhne, P. Esquinazl, Y. Kopelevich, P. Scharff, V. Davydov, L. Kashevarova, and A. Rakhmanina, Nature **413,** 716 (2001).

[14] A. V. Rode, E. G. Gamaly, A. G. Christy, J. G. Fitz Gerald, S. T. Hyde, R. G. Elliman, B. Luther-Davies, A. I. Veinger, J. Androulakis, and J. Giapintzakis, Phys. Rev. B **70,** 054407 (2004).

[15] T. L. Makarova, "Magnetism of carbon-based materials," in *Studies of High-Temperature Superconductivity*, A. Narlikar, ed., (Nova Science, Huntington, New York, 2003), Vol. 45, Chap. 7, p. 107, and references therein.

[16] P. Esquinazi, A. Setzer, R. Höhne, C. Semmelhack, Y. Kopelevich, D. Spemann, T. Butz, B. Kohlstrunk, and M. Lösche, Phys. Rev. B **66,** 024429 (2002).

[17] T. L. Makarova, J. Magnetism and Magnetic materials **272-276,** E1263 (2004).

[18] M. Fujita, K. Wakabayashi, K. Nakada, and K. Kusakabe, J. Phys. Soc. Jpn. **65,** 1920 (1996).

[19] Y. Shibayama, H. Sato, T. Enoki, and M. Endo, Phys. Rev. Lett. **84,** 1744 (2000).

[20] K. Nakada, M. Fujita, G. Dresselhaus, and M. S. Dresselhaus, Phys. Rev. B **54,** 17954 (1996).

[21] A. N. Andriotis, M. Menon, R. M. Sheetz, and L. Chernozatonskii, Phys. Rev. Lett. **90,** 026801 (2003).

[22] K. Kusakabe and M. Maruyama, Phys. Rev. B **67,** 092406 (2003).

[23] Y.-H. Kim, J. Choi, K. J. Chang, and D. Tománek, Phys. Rev. B **68,** 125420 (2003).

[24] D. V. Khveshchenko, Phys. Rev. Lett. **87,** 206401 (2001).

[25] D. V. Khveshchenko, Phys. Rev. Lett. **87,** 246802 (2001).

[26] N. Park, M. Yoon, S. Berber, J. Ihm, E. Osawa, and D. Tománek, Phys. Rev. Lett. **91,** 237204 (2003).

[27] J. A. Chan, B. Montanari, J. D. Gale, S. M. Bennington, J. W. Taylor, and N. M. Harrison, Phys. Rev. B **70,** 041403 (2004).

[28] S. Okada and A. Oshiyama, J. Phys. Soc. Jpn. **72,** 1510 (2003).

[29] P. Esquinazi, D. Spearmann, R. Höhne, A. Setzer, and T. Butz, Phys. Rev. Lett. **91,** 227201 (2003).

[30] H. Dorsett and A. White, *Overview of Molecular Modelling and Ab initio Molecular Orbital Methods Suitable for Use with Energetic Materials* (DSTO Aeronautical and Maritime Research Laboratory, Salisbury, 2000).

[31] G. C. Schatz, Rev. Mod. Phys. **61,** 669 (1989).

[32] R. M. Dreizler and E. K. U. Gross, *Density Functional Theory* (Springer-Verlag, Berlin, 1990).

[33] P. Hohenberg and W. Kohn, Phys. Rev. **136,** B864 (1964).

[34] W. Kohn and L. J. Sham, Phys. Rev. **140,** A1133 (1965).

[35] W. Kohn, Rev. Mod. Phys **71,** 1253 (1999).

[36] S.-K. Ma and K. A. Brückner, Phys. Rev. **165,** 18 (1968).

[37] E. K. U. Gross, E. Runge, and O. Heinonen, *Many-Particle Theory* (Adam Hilger, Bristol, 1991).

[38] M. Gell-Mann and K. A. Brueckner, Phys. Rev. **106,** 364 (1957).

[39] U. von Barth and L. Hedin, J. Chem. Phys. C **5,** 1629 (1972).

[40] E. P. Wigner, Phys. Rev. **46,** 1002 (1934).

[41] E. P. Wigner, Trans. Farad. Soc. **34,** 678 (1938).

[42] W. J. Carr, R. A. Coldwell-Horsfall, and A. E. Fein, Phys. Rev. **124,** 747 (1961).

[43] J. Perdew and A. Zunger, Phys. Rev. B **23,** 5048 (1981).

[44] D. M. Ceperley and B. J. Alder, Phys. Rev. Lett. **45,** 566 (1980).

[45] J. P. Perdew and Y. Wang, Phys. Rev. B **33,** 8800 (1986).

[46] J. P. Perdew, K. Burke, and Y. Wang, Phys. Rev. B **54,** 16533 (1996).

[47] J. P. Perdew, J. A. Chevary, S. H. Vosko, K. A. Jackson, M. R. Pederson, D. J. Singh, and C. Fiolhais, Phys. Rev. B **46,** 6671 (1992).

[48] J. P. Perdew, in *A Primer in the density functional theory*, C. Fiolhais, F. Nogueira, and M. Marques, eds., (Springer, Berlin, New York, 2003).

[49] W. Kohn, Y. Meir, and D. E. Makarov, Phys. Rev. Lett. **80,** 4153 (1998).

[50] H. Rydberg, M. Dion, N. Jacobson, E. Schröder, P. Hyldgaard, S. I. Simak, D. C. Langreth, and B. I. Lundqvist, Phys. Rev. Lett. **91,** 126402 (2003).

[51] R. W. Godby, M. Schlüter, and L. J. Sham, Phys. Rev. Lett. **56,** 2145 (1986).

[52] C. Stampfl and C. G. V. de Walle, Phys. Rev. B **59,** 5521 (1999).

[53] N. W. Ashcroft and N. D. Mermin, *Solid State Physics* (Thomson Learning, Pacific Grove, Belmont, 1976).

[54] H. Monkhorst and J. Pack, Phys. Rev. B **13,** 5188 (1976).

[55] M. C. Payne, M. P. Teter, D. C. Allan, T. A. Arias, and J. D. Joannopoulos, Rev. Mod. Phys. **64,** 1045 (1992).

[56] P. E. Blöchl, Phys. Rev. B **50,** 17953 (1994).

[57] G. Kresse and D. Joubert, Phys. Rev. B **59,** 1758 (1999).

[58] H. Hellmann, *Einführung in die Quantumchemie* (Deuticke, Leipzig, 1937).

[59] R. P. Feynman, Phys. Rev. **56,** 340 (1939).

[60] G. Kresse and J. Fürthmüller, *VASP the Guide* (http://cms.mpi.univie.ac.at/VASP/, 2003).

[61] G.Kresse and J. Furthmüller, Comp. Mat. Sci. **6,** 15 (1996).

[62] G.Kresse and J. Furthmüller, Phys. Rev. B **54,** 11169 (1996).

[63] A. J. Stone and D. J. Wales, Chem.Phys.Lett. **128,** 501 (1986).

[64] C. P. Ewels, M. I. Heggie, and P. R. Briddon, Chem. Phys. Lett. **351,** 178–182 (2002).

[65] A. V. Krasheninnikov, K. Nordlund, M. Sirviö, E. Salonen, and J. Keinonen, Phys. Rev. B **63,** 245405 (2001).

[66] A. V. Krasheninnikov, K. Nordlund, and J. Keinonen, Phys. Rev. B **65,** 165423 (2002).

[67] K.Nordlund, J.Keinonen, and T. Mattila, Phys. Rev. Lett. **77,** 699 (1996).

[68] P. O. Lehtinen, A. Foster, A. Ayuela, A. Krasheninnikov, K. Nordlund, and R. M. Nieminen, Phys. Rev. Lett. **91,** 017202 (2003).

[69] M. Heggie, Electrochemical Society Proceedings **98,** 60 (1997).

[70] Y. H. Lee, S. G. Kim, and D. Tománek, Phys. Rev. Lett. **78,** 2393 (1997).

[71] F. Banhart, Rep. Prog. Phys. **62,** 1181 (1999).

[72] P. O. Lehtinen, A. S. Foster, A. Ayuela, T. T. Vehviläinen, and R. M. Nieminen, Phys. Rev. B **69,** 155422 (2004).

[73] A. V. Krasheninnikov, K. Nordlund, P. Lehtinen, A. Foster, A. Ayuela, and R. Nieminen, Phys. Rev. B **69,** 073402 (2004).

[74] G.-X. Qian, R. M. Martin, and D. J. Chadi, Phys. Rev. B **38,** 7649 (1988).

[75] E. Kaxiras and K. Pandey, Phys. Rev. Lett. **72,** 1878 (1988).

[76] A. A. El-Barbary, R. H. Telling, C. P. Ewels, M. I. Heggie, and P. R. Briddon, Phys. Rev. B **68,** 144107 (2003).

[77] Y. Ma, P. O. Lehtinen, A. S. Foster, and R. M. Nieminen, New J. Phys. 6 (2004).

[78] R. Telling, C. Ewels, A. El-Barbary, and M. Heggie, Nature Materials **2,** 333 (2003).

[79] E. Kaxiras and K. Pandey, Phys. Rev. Lett. **61,** 2693 (1988).

[80] C. Xu and D. Pedraza, Phys. Rev. B **48,** 13273 (1993).

[81] P. A. Thrower and R. M. Mayer, Phys. Stat. Sol. (a) **47,** 11 (1978).

[82] S. Okada and A. Oshiyama, Phys. Rev. Lett. **87,** 146803 (2001).

[83] Y. Ferro, F. Marrinelli, and A. Allouche, J. Chem. Phys. **116,** 8124 (2002).

[84] Y. Ferro, F. Marrinelli, and A. Allouche, Chem. Phys. Lett. **368,** 609 (2003).

[85] E. J. Duplock, M. Scheffler, and P. J. D. Lindan, Phys. Rev. Lett. **92,** 225502 (2004).

[86] X. Sha and B. Jackson, Surf. Sci. **496,** 318 (2002).

[87] P. Ruffieux, O. Gröning, P. Schwaller, L. Schlapbach, and P. Gröning, Phys. Rev. Lett. **84,** 4910 (2000).

[88] A. Hashimoto, K. Suenaga, A. Gloter, K. Urita, and S. Iijima, Nature **420,** 870 (2004).

[89] R. K. Pathria, *Statistical Mechanics* (Butterworth-Heinemann, Oxford, 1996).